

Development of thick GaN and AlGaN drift layers for vertical power devices

Andri Dhora



LUND
UNIVERSITY

Department of Solid State Physics

MSc Thesis TFRT-9999
ISSN 0280-5316

Department of Solid State Physics
Lund University
Box 118
SE-221 00 LUND
Sweden

© 2023 by Andri Dhora. All rights reserved.
Printed in Sweden by Media-Tryck.
Lund 2023

Abstract

High-quality, thick III-nitride epitaxial drift layers with controlled doping are needed for next-generation highly efficient vertical power devices for a smart grid applications and electrification of mobility. Achieving desirable material properties, such as low background impurity concentrations and reduced dislocation densities in combination with high growth rates, necessary for practical application present a challenge. In this work, metal-organic vapor phase epitaxy (MOVPE) is employed for the development of GaN and low-Al content AlGaN drift layers on GaN substrates.

GaN drift layers with controlled Si doping of $4.6 \times 10^{16} \text{cm}^{-3}$ and thicknesses of $5 \mu\text{m}$ and $10 \mu\text{m}$ were homoepitaxially grown utilizing a n^+ ($7.6 \times 10^{18} \text{cm}^{-3}$) 300 nm-thick GaN nucleation layers. Smooth surface layer morphology with a surface roughness of 0.11 nm over $2 \mu\text{m} \times 2 \mu\text{m}$ area was demonstrated and the density of screw dislocations in the drift layers was found to be comparable to or better than that in the GaN substrate. In addition, the densities of edge dislocations, which are the predominant type of dislocations and are responsible for the undesired leakage currents, were decreased with respect to the substrate. At the optimised growth conditions, an industrially relevant growth rate of $2 \mu\text{m}/\text{h}$ was achieved, and background concentrations of C, H and O were limited to $1.1 \times 10^{16} \text{cm}^{-3}$, $3.4 \times 10^{16} \text{cm}^{-3}$ and $9.6 \times 10^{14} \text{cm}^{-3}$, respectively.

To enhance the Baliga figure of merit, $5 \mu\text{m}$ AlGaN drift layers with low Al content (7.28%) were grown on GaN substrates. A graded AlGaN buffer layer was developed to accommodate tensile strain, where both its thickness and doping were explored. We found that a 300 nm thick, n^- doped, compositionally-graded AlGaN buffer layer enables crack-free drift layers with smooth surface morphology (surface roughness of 0.15 nm). As a next step the optimized GaN and AlGaN drift layers are being employed for the fabrication of FIN field effect transistors.

Acknowledgements

This thesis would not have been possible without the work of Byeongchan So.

I am indebted to Vanya Darakchieva for her guidance, courage and for taking me under her wings. Special thanks to the incredible Alexis Papamichail - thank you for bearing with me for four intense days.

Thank you, Peter Blomqvist, for training me on the instruments, and for patiently fixing the broken ones; including the ones that I broke.

Thank you, Jovana Colvin, for sharing the vital sample cleaning secrets.

L.H, Y.J, *zemra ime*, my light. I love you.

Contents

1. Introduction	9
1.1 Background and motivation	9
1.2 Challenges and objectives	11
2. Group-III nitrides	13
2.1 Chemical bonding and crystal structure	13
2.2 AlGaN alloys	15
2.3 Polarity	15
2.4 Spontaneous and piezoelectric polarizations	16
2.5 Point defects and doping	17
2.6 Material properties relevant to power electronics	19
2.7 Strain and dislocations	20
2.8 Substrates for GaN homo- and hetero-epitaxy	24
3. MOVPE	27
3.1 General concepts	27
3.2 Growth regimes	29
3.3 Close-coupled showerhead (CCS) MOVPE system	31
4. Characterization methods	36
4.1 X-ray diffraction	36
4.2 Atomic force microscopy	42
4.3 Secondary ion mass spectroscopy	43
4.4 Scanning electron microscopy (SEM)	44
4.5 X-ray energy dispersive spectroscopy (EDS)	46
5. Results and Discussion	47
5.1 Growth optimization	47
5.2 GaN and AlGaN epitaxy	53
5.3 Structural properties of the drift layers	58
6. Summary and outlook	64
Bibliography	66

1

Introduction

1.1 Background and motivation

As our world's energy demands continue to rise, there is a growing need for energy-efficient power electronic components such as converters, in order to optimise the use of energy and minimize waste. It is projected that by the next decade, roughly 80% of generated electricity will pass through multiple power conversion stages on the way to the consumers [1], which requires the development of next-generation highly efficient power rectifiers and switches handling high currents and high breakdown voltages.

Power electronics is the field that seeks efficient conversion of electrical power by use of e.g., electronic switches and rectifiers [2]. Two main categories of power electronic devices exist in terms of the direction of current flow; in lateral power devices the current flows parallel to the surface, while in vertical power devices the current flows vertically through the bulk. In vertical power devices, higher voltages in reverse-biased conditions can be withstood compared to their lateral counterparts, and operation at higher current levels is possible. In addition, vertical architectures offer better thermal dissipation and allow for smaller chip size. Consequently, vertical architectures allow for a more efficient use of energy and lower device cost.

A variety of device architectures have been developed for vertical power devices, however they share the same fundamental epitaxial structure comprised of a typically n^+ substrate, a lightly doped epitaxially grown region - often referred to as the *drift layer* - through which the current flows vertically in the direction of epitaxial growth, and a top-layer that can be processed to form the channel and junctions. The drift layer is typically a few microns long to enable higher voltage-blocking ability, at the evident expense of a larger voltage drop in forward bias. In the ideal scenario, for higher efficiency, a low Ohmic resistance for majority carriers in the ON state alongside high voltage-blocking ability in the OFF state are desired.

Silicon (Si) has been dominating power electronics for many decades. The ability to grow single crystalline material with high purity and precisely control its conductivity via selective doping have laid the foundations for silicon to become the backbone of modern technology. Among its other key advantages, are the low cost, relative abundance, and the existence of a native oxide, which can be utilised as a

gate dielectric and / or for passivation.

For power devices however, the theoretical performance limits of Si-technology have already been reached [3]. The use of wide bandgap semiconductors (WBGs) for power devices, such as SiC, GaN and AlN, presents multiple advantages over Si. WBG semiconductors can enable higher maximum operating temperatures, higher breakdown voltages and lower ON-state resistance for a given drift layer thickness and doping level, thanks to their higher electron mobility and critical field at breakdown. This can be illustrated by considering the link between the breakdown voltage V_{br} to the material constant E_c - the critical electric field at avalanche breakdown, and to the two design parameters, the width of the drift layer, W_b , and the net doping concentration of the drift layer N_d . In the ideal case of a triangular electric field profile in the drift region, $V_{br} = E_c W_b / 2$ where $W_b \propto E_c / N_d$. Therefore, for a given material, the only way to increase the breakdown voltage for a vertical power device is through a lower doped and thicker drift layer, at the expense of a higher ON resistance, R_{ON} , since $R_{ON} \propto \rho \frac{W_b}{A} \propto \frac{W_b}{\mu N_d} \propto \frac{V_{br}^2}{\epsilon \mu E_c^3}$, where ϵ is the dielectric permittivity and μ the mobility of the majority carriers. The critical electric field obeys a power law dependence on the bandgap, with $E_c \propto E_g^{2.5}$ for direct bandgap semiconductors. Due to its low bandgap of 1.14 eV at room temperature, Si has consequently a small critical electric field and the R_{ON} - breakdown - voltage trade-off becomes particularly evident, which is the main limitation for vertical devices in Si-based power electronics.

The use of WBG semiconductors allows for a softer trade-off. This idea was first proposed by Baliga, and the factor $\epsilon \mu E_c^3$ is duly referred to as the Baliga figure of merit – a quantitative unit to evaluate the relative performance of vertical power devices in terms of their material parameters – originally defined as $\epsilon \mu E_g^3$ [4]. GaN for instance has BFOM a factor of about 1230 higher than Si; in addition to lower R_{ON} , this reduces the necessary thickness of the drift layer by orders of magnitude for a given breakdown voltage, resulting in more compact devices with higher energy efficiency (up to 99% or better - [5]). The wider bandgap allows for higher breakdown voltages at shorter drift layer thicknesses, permitting the blocking of greater voltages when the switch is off.

Since the intrinsic free charge carrier concentration in semiconductors decreases exponentially with bandgap, wider bandgap semiconductor have significantly lower intrinsic charge at a given temperature, allowing for a higher working temperatures (above 500°C) compared to Si MOSFETs for instance (150°C[5]) in principle. In addition, Si has a poor thermal performance due to its inferior thermal conductivity. As a result of the multiple material advantages, WBG semiconductors have attracted significant research and industrial interest in relation to developing next generation highly efficient power electronic devices and components.

1.2 Challenges and objectives

Despite intense research efforts in the field of GaN material technology for power electronics, there are numerous challenges that need to be addressed in order to fully exploit the material potential. One of the main current obstacles is realising epitaxial GaN with low defect densities due to the lack of low-cost native substrates. GaN and AlN bulk crystallization from a stoichiometric melt by use of classical methods - such as the Czochalski or the Bridgman method - requires extreme growth conditions, as GaN and AlN melt at about 2500°C and 2200°C respectively, and nitrogen has a dissociation pressure of about 6 GPa at these melting temperatures [6]. As a result, typically, III-nitrides are heteroepitaxially grown on foreign substrates of relatively low-cost - such as Si, SiC and Sapphire.

In such instances, the mismatch in lattice constants and thermal expansion coefficients between the layers and the substrate leads to strain and a relatively high density of threading dislocations (TDD). TDDs along with other defects form an unwanted source of charge carrier scattering and therefore of leakage currents; which must be minimised in order to utilise in full the advantages of III-nitrides for vertical power devices [7]. Typical TDD are of the order of $10^9 - 10^{10} \text{cm}^{-2}$ for GaN-on-Si and GaN-on-Sapphire and $10^8 - 10^9 \text{cm}^{-2}$ for GaN-on-SiC [8] [9].

Homoepitaxial GaN growth can allow for drastic minimization of dislocation densities and has been realized using GaN substrates that are grown either ammonothermally [10] or by hydride vapour phase epitaxy (HVPE) [11]. Homoepitaxial GaN on HVPE substrates results in epilayers with TDDs of the order 10^6cm^{-2} ; a factor of about 5-10 lower than the typical TDDs in heteroepitaxially-grown GaN layers on SiC substrates for instance. Large-scale commercialisation of devices based on homoepitaxially-grown GaN is currently hampered by the price of the HVPE-grown GaN wafers (about 500\$/ cm^{-2}). However, it is anticipated that the large demand will drive down the cost of GaN substrates in the near future.

Good control of the thickness and net doping in the drift layers is paramount to achieve the highest voltage theoretically possible for a given material. Drift layers in vertical GaN power devices are typically grown by metal-organic vapour-phase epitaxy (MOVPE), that inevitably introduces incorporation of impurities such as hydrogen, oxygen and carbon, as a result of the metal-organic source for Gallium. Carbon is an amphoteric dopant in GaN, but in n-type material it introduces deep acceptor states by occupying nitrogen sites [12] thereby compensating intentional n-type doping. The concentration of unintentional impurities can, to a certain extent, be limited by working at high growth temperatures, high pressures and high III/V ratios (see for further details Section 5.1), however, this results in an undesired decrease of the growth rate [13].

Therefore, the main scientific challenges that this work has aimed to tackle revolve around the development of appropriate approaches to optimise the properties of

GaN and AlGa_N drift layers on GaN substrates at sufficiently high growth rates for their implementation in power devices. They may be summarized as follows:

- (i) Development of high-quality, thick (i.e., above $5\mu\text{m}$) and crack-free GaN and AlGa_N drift layers by MOVPE, to enable higher breakdown voltages for power devices.
- (ii) Optimization of growth variables to limit the Carbon-concentration below 10^{16}cm^{-3} , while maintaining a reasonably fast growth rate.
- (iii) Minimization of TDDs by limiting them to an upper threshold of 10^6cm^{-2} .
- (iv) Minimization of the surface roughness to root mean square (RMS) values of the order $\sim 0.1\text{nm}$.

2

Group-III nitrides

2.1 Chemical bonding and crystal structure

Group III-nitrides (GaN, AlN, InN and their alloys) are direct bandgap semiconductors. The stronger electronegativity of Nitrogen compared to the rest of the group V elements, gives rise to a predominantly ionic bond between the group-III cations and Nitrogen anion. This ionic bond is energetically stronger as compared to the covalent and partially ionic bonds of the corresponding group III-arsenides or III-phosphites, for instance. In addition, the smaller covalent radius of Nitrogen allows for comparatively smaller lattice constants. These two factors account for the high chemical and thermal stability, and the variation in bandgaps across a wide range: from the ultrawide bandgap of AlN (6.14 eV [14]), to the wide bandgap of GaN (3.43 eV [14]), and the narrow bandgap of InN (0.64 eV [15])¹.

III-nitrides can crystallize in either the wurtzite (WZ), zincblende (ZB) or the rock-salt (RS) crystal structures. The wurtzite structure is the thermodynamically stable structure, while the latter two are metastable; where the rocksalt crystal structure requires higher pressure conditions in order to be stabilised [17]. Hence, wurtzite GaN, In and AlN are encountered more frequently in practice. In the remaining part of the thesis we only refer to wurtzite III nitrides.

The wurtzite unit cell – shown in Figure 2.2 for GaN – is composed of two alternating hexagonal close-packed (hcp) sublattices; one consisting of nitrogen anions N^{3-} the other of group-III cations ($Al^{3+}, Ga^{3+}, In^{3+}$). Each nitrogen atom is surrounded by three group III atoms, forming a trigonal pyramid, while each Group III atom is coordinated to four nitrogen atoms. The wurtzite structure is described by the lattice constant perpendicular to the hexagonal unit cell, c , (i.e., along the [0001] direction, or the c -axis), and two in-plane (basal plane) lattice constants a and b , equal in length. The parameter that characterizes the distance between the two interlocking sublattices is the internal wurtzite structure parameter, u , given by the ratio of the anion-cation bond length to the lattice constant c . In the ideal wurtzite unit cell, $u = 3c/8$ and $\frac{c}{a} = \sqrt{8/3}$. However, deviations occur due to the strong III-N ionic bonds, that distort the unit cell slightly [19] (Table 2.1).

¹ Note that these are the room temperature bandgap values.

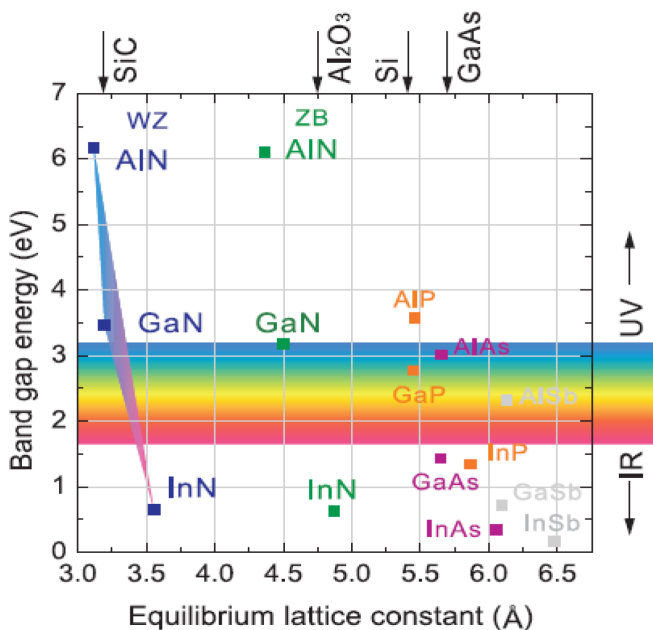


Figure 2.1 Room temperature bandgaps of III-nitrides in their Wurtzite and Zincblende structures and those of the corresponding III-arsenides, III-phosphides and III-antimonides, plotted versus the respective in-plane lattice constant. The lattice constants of SiC, sapphire, Si and GaAs, commonly used as substrates, are also indicated [16].

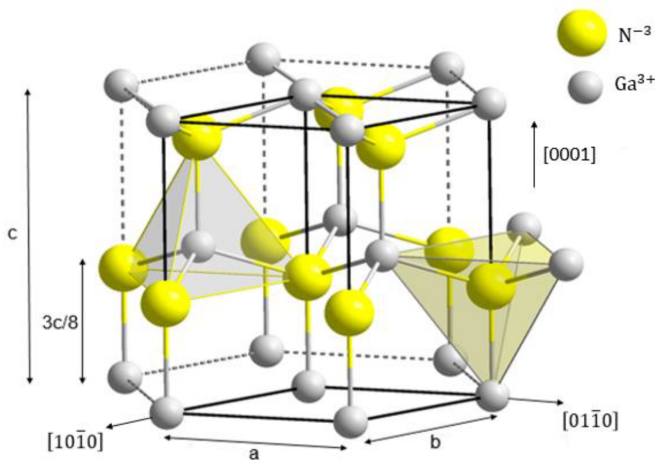


Figure 2.2 Wurtzite unit cell of GaN. From [18]

Table 2.1 Lattice constants, internal structure parameters and bandgap energy values at zero Kelvin for WZ III-nitrides.

	Lattice constant (Å) [20]		Internal Parameter [21]	E _g (T=0K) (eV) [14]
	a	c	u	E _g
GaN	3.189	5.185	0.376	3.51
AlN	3.112	4.982	0.380	6.25
InN	3.533	5.693	0.377	0.69

2.2 AlGa_N alloys

AlN and GaN are miscible at all temperatures and compositions, thanks to the absence of a miscibility gap [22]. For calculations of the lattice parameters of III-nitride alloys, a linear relation between alloy composition and lattice constant can be assumed (Vegard's rule [23]), yielding, for example the ternary Al_xGa_{1-x}N alloy, a lattice parameter of

$$a_{\text{Al}_x\text{Ga}_{1-x}\text{N}} = xa_{\text{AlN}} + (1-x)a_{\text{GaN}} \quad (2.1)$$

where a_{AlN} , a_{GaN} , and x , are the lattice constants of GaN, AlN and the molar fraction of AlN in Al_xGa_{1-x}N, respectively.

For Al_xGa_{1-x}N, the bandgap exhibits a non-linear dependence of the molar fraction of AlN, expressed by the empirical relation [24]:

$$E_g(\text{Al}_x\text{Ga}_{1-x}\text{N}) = xE_g(\text{AlN}) + (1-x)E_g(\text{GaN}) - bx(1-x) \quad (2.2)$$

where $E_g(\text{AlN})$ and $E_g(\text{GaN})$ are the bandgaps for AlN and GaN, respectively, and b is the so called bowing parameter, which quantifies the deviation from Vegard's rule. The value of b is a function of the accumulated strain in AlGa_N epilayers; itself a function of the growth conditions, substrate and epilayer thickness [25] AlGa_N alloys permit tailoring the bandgap in the range 3.4 eV - 6.2eV as shown in Figure 2.1.

2.3 Polarity

Wurtzite III-nitride crystals are polar, due to the lack of inversion centre perpendicular to the c-axis. In other words, their surfaces are said to be either group-III polar (or Ga-, Al-, In-polar), or N-polar (or N-polar) in a given direction. By convention, the material is N-polar if the triple bonds of the group-III atom are oriented along the $[000\bar{1}]$ axis and metal-polar if oriented along the $[0001]$ axis (Figure 2.3). Polarity is an important material property that affects the surface morphology of epilayers, concentration of defects and dopant incorporation [26], and can be controlled by the substrate orientation and/or the growth conditions. For MOVPE growth of smooth GaN epilayers, Ga-polar substrates are used, as also implemented in this thesis.

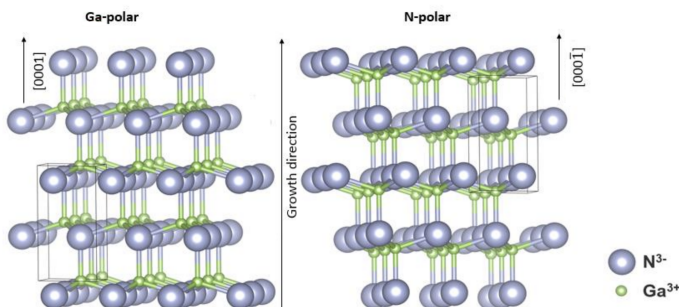


Figure 2.3 Schematic of a wurtzite GaN lattice depicting Ga-polar GaN (left) and a N-polar (right) in the $\langle 0001 \rangle$ direction. The growth direction is indicated [16].

2.4 Spontaneous and piezoelectric polarizations

Due to the higher electronegativity of N-atoms relative to group-III atoms, each III-N bond behaves like an electric dipole, with the field pointing from the metal atom towards the Nitrogen atom, with the dipole moment conventionally oriented in the opposite direction. In an ideal wurtzite unit cell, $\frac{c}{a} = \sqrt{8/3}$; as a result the individual tetrahedral molecules have bond angles $\alpha = \beta = 109.47$ [19], thus the vertical and in-plane dipole moment components would vanish. For III-nitrides, distortions of the unit cell due to the strong electronegativity differences between atoms lead to $\alpha < \beta$, giving rise to an overall vertical microscopic polarization \vec{P} in each tetrahedron, that points from Nitrogen to the metal atom as shown in Figure 2.4 below.

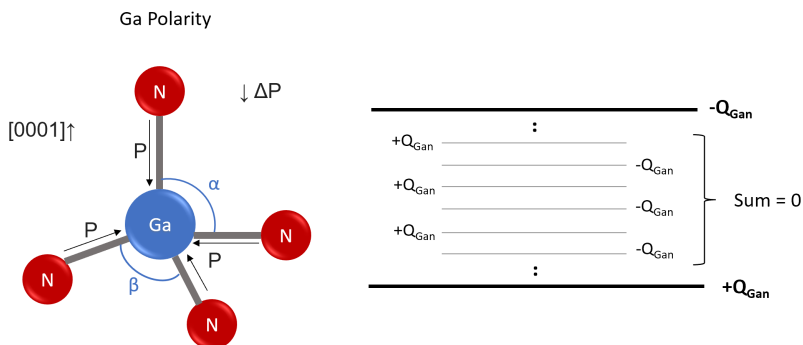


Figure 2.4 A strain-free GaN tetrahedron exhibiting net spontaneous polarization (left). Diagram depicting the induced surface polarization charge in GaN (right).

As a result, a corresponding macroscopic polarization is observed – called ‘spontaneous’, since it occurs in strain-free conditions – defined as the spontaneous dipole moment per unit volume, $\vec{P}_{SP} = n \langle \vec{p} \rangle$ where n is the number of dipoles per unit vol-

ume, and $\langle \vec{p} \rangle$ the average dipole moment associated with the individual (non-ideal) tetrahedral III-nitride molecules. The magnitude of the spontaneous polarization, $|\vec{P}_{SP}|$, depends on the electronegativity difference between the N- and group-III atoms (Al, Ga, In) that determines the extent of distortion of the ideal wurtzite unit cell, while its direction is determined by the polarity of the material; \vec{P}_{SP} points along the $[000\bar{1}]$ direction for metal-polar surfaces and along $[0001]$ for N-polar surfaces.

As a result of the spontaneous polarization - though there will be no net charge in the bulk, due to moments cancelling out between neighboring dipoles - positive and negative surface charges are induced on the N- and metal-terminated faces, respectively, even in unstrained and defect-free III-nitride materials. These polarization induced surface charges are what enable the formation of two-dimensional electron gas (2DEG) in AlGaIn/GaN high mobility transistors (HEMTs).

In addition to the macroscopic spontaneous polarization, a piezoelectric polarization \vec{P}_{PZ} is also present in AlGaIn/GaN heterostructures as a result of the strain that derives from the mismatch in lattice constants between the layers. The magnitude of \vec{P}_{PZ} will depend on the piezoelectric and elastic coefficients of the alloy [27], while its direction depends on the nature of the strain (i.e., whether it is tensile or compressive) and on the polarity of the substrate. For instance, for AlGaIn growth on thick Ga-polar GaN substrate, the epilayer will be under tensile stress due to the smaller in-plane lattice constant of AlGaIn relative to GaN. As a result the polarization components of the triple bonds in vertical direction will decrease, producing a piezoelectric polarization parallel to \vec{P}_{SP} .

2.5 Point defects and doping

The intrinsic carrier concentration (n_i) in a bulk (3D) semiconductor is a thermally-activated process that depends on the bandgap E_g and the effective density of states in the conduction band (N_C) and the valence band (N_V) via the relation $n_i = \sqrt{N_C N_V} \exp(-E_g/2kT)$, where k and T are the Boltzmann's constant and the temperature, respectively. The intrinsic carrier concentration in GaN and AlN practically vanishes at room temperature thanks to the large bandgap.

To control the conductivity of semiconductors, intentional impurity atoms with different valence states to host atoms are introduced in the lattice to replace some of the host atoms - a process called *doping* [28]. Doping necessarily leads to the formation of localized imperfections in the ideal crystal lattice (i.e., *extrinsic* point defects) due to the difference in properties of the host atoms and impurity atoms.

For *p-type* doping in GaN, group-II atoms are intentionally incorporated into the lattice to substitute for group-III atoms. *N-type* doping is achieved by intentional impurity group-IV atoms substituting for group-III atoms. Group-IV atoms intro-

duce donor energy levels in the bandgap for extra electrons, while group-II atoms introduce acceptor energy levels for holes. The impurity donor/acceptor states are called shallow if their ionization energies are well approximated by the hydrogenic approximation; which in a bulk crystal reads, $E_i \approx 13.6\text{eV} \times m_{e,h}^* / \epsilon_r^2 m_0$, where m_e^* , m_h^* and m_0 are the effective masses for holes, electrons, and the free carrier mass respectively, and ϵ_r the relative permittivity for the material. In GaN ($\epsilon_r = 10.4$, $\frac{m_e^*}{m_h} \approx 0.2$, $\frac{m_h^*}{m_h} \approx 1.2$) shallow donors have energies of about 25meV below the conduction band, while shallow acceptors 150meV above the valence band. Under sufficient thermal energy, the electrons (holes) are excited up (down) to the conduction band (valence band), realising a n-type (p-type) semiconductor.

In choosing an appropriate dopant (substitutional impurity atom) for a given semiconductor, in addition to the ionization energy of its impurity states, its solubility and diffusivity in the material, must also be considered. Silicon, if substitutional for Ga (Si_{Ga}) in GaN, creates a shallow donor state 27meV below the bottom of the conduction band [29], and is more soluble than other possible donors (Ge, Se) of larger atomic radii. As a result, Si is the dopant of choice for n-type GaN. P-type doping in GaN is more challenging. It is achieved through doping by Mg, which acts as a *shallow* acceptor, creating acceptor states with ionization energies of about 200meV. As a result, only a fraction of holes are activated at room temperature.

MOVPE grown GaN is always unintentionally doped (UID-GaN,) however. As a result, intentional doping is always enhanced or compensated. This occurs due to a combination of:

- (a) the incorporation of residual (impurity) atoms during MOVPE growth
- (b) the formation of *intrinsic* (or native) point defects in the lattice, such as Gallium vacancies (V_{Ga}), Nitrogen vacancies (V_{N}), interstitials (atoms occupying non-lattice positions) that necessarily occur at finite temperature to minimize the Gibbs free energy of the system.

The unintentional impurities in MOVPE growth are referred to as background (or residual) impurities, and include O, H, C, and Si. They create energy bands at either the deep or shallow donor (acceptor) level, thereby compensate intentional acceptors (donors). Deep states acts as electron traps, enabling to leakage current and low resistance in the ON state [30]. Background impurity concentrations are highly sensitive to the growth conditions; the latter must be optimised to minimize their incorporation.

Incorporation of background O in UID-Gan layers occurs when TMGa and NH_3 precursors are exposed to Oxygen from any oxide present in the reactor parts, and the water that infiltrates the chamber during loading / unloading of the samples. It can be minimized to values of 10^{15} cm^{-3} by lowering the reactor pressure down to high-vacuum levels (10^{-5} mbar) prior to growth. Atomic hydrogen is introduced

Table 2.2 Room-temperature physical properties relevant for power electronics for major semiconductor materials: Si, SiC, GaN, AlN, $\beta - \text{Ga}_2\text{O}_3$ and Diamond. The critical field values assume $N_d = 10^{16} \text{cm}^{-3}$.

Material	Bandgap (eV)	Relative permittivity	Electron mobility ($\text{cm}^2\text{V}^{-1}\text{s}^{-1}$)	Critical field (MVcm^{-1})	Thermal conductivity ($\text{Wm}^{-1}\text{K}^{-1}$)	con-	BFOM = $\frac{1}{4}\epsilon\mu E_c^3(10^{20}\text{V}^2\text{s}^{-1}\text{cm}^{-1})$
Si	1.1	11.9	1300	0.3	130		1
SiC [32],[33],[34]	3.3	9.7	800	2.5	490		303
GaN [35],[33],[36],[37]	3.4	10.4 (\parallel to c-axis)	1200	3.4	230		1230
AlN [32],[33]	6.3	9.14	300	12	270		11850
$\beta - \text{Ga}_2\text{O}_3$ [32]	4.9	16.3	150	10.3	27		6680
Diamond [32]	5.5	5.7	2000	13	2290		62620

from the dissociation of molecular hydrogen (an important carrier gas in MOVPE), NH_3 and metal-organic (MO) precursors. The most important source of background C derives from the dissociation of the CH_3 ligands present in TMGa. Sources of Si include the SiC-coated graphite susceptor. The purity of the precursors is also important to minimise O and Si concentrations.

In UID-GaN, C acts like an *amphoteric* dopant; it behaves as a shallow acceptor if substituted to a Nitrogen site (C_N), and acts as a deep donor if substituted to a Ga site (C_{Ga}). In n-type GaN, C acts as a deep acceptor, compensating intentional Si (n-type) doping [12]. Similar to background Si, Oxygen introduces shallow donor states (27meV) via substitution for N atoms. These are activated at room temperature and serve to unintentionally dope GaN or enhance its intentional n-type doping. H behaves as an acceptor in n-GaN, however, despite its high abundance in MOVPE growth, its incorporation in n-GaN is limited due to the high energy needed for the formation of this substitutional defect [31].

While in theory GaN can be doped up to $\approx 10^{22} \text{cm}^{-3}$, compensation due to native defects limit the possible doping concentrations to below this upper limit [32]. Native defects such as vacancies (V_{Ga}), Nitrogen vacancies (V_N), also serve to introduce trap states in the bandgap and thereby compensate intentional doping to varying degrees (depending on whether they are shallow or deep) [3]. V_N and V_{Ga} act as a shallow donor and deep acceptor, respectively being the most common native defect in GaN, thanks to its relatively lower formation energy.

2.6 Material properties relevant to power electronics

Table 2.2 summarizes the material properties of major semiconductor materials relevant for power electronics. The WBG SiC ($E_g = 3.3 \text{ eV}$) and GaN ($E_g = 3.4 \text{ eV}$) have high critical electric fields and hence they exhibit significantly higher Baliga Figure of Merit (BFOM) compared to Si. Since the BFOM is defined as $\frac{V_{br}^2}{R_{on}}$ or $\frac{1}{4}\epsilon\mu E_c^3$, this translates to the ability to block higher voltages in the off-state and offer better conductivity in the on-state for power devices.

SiC technology is more established in power device applications compared to GaN. SiC has a higher thermal conductivity than GaN, similar bandgap, and is more cost-

effective. However, GaN shows more promise for power devices due to its larger critical field and higher electron mobility, resulting in four times higher BFOM. Other materials with higher bandgap, such as diamond, AlN/AlGaN and Ga₂O₃, are categorized as ultra-wide bandgap (UWBG) materials. They possess substantially larger BFOMs, promising even better performance in power electronic applications.

The relationship between BFOM, R_{ON} and V_{br} for the main semiconductors is illustrated in Figure 2.5. Contours of constant BFOM are plotted, where a larger BFOM indicates a higher breakdown voltage for a given ON-resistance.

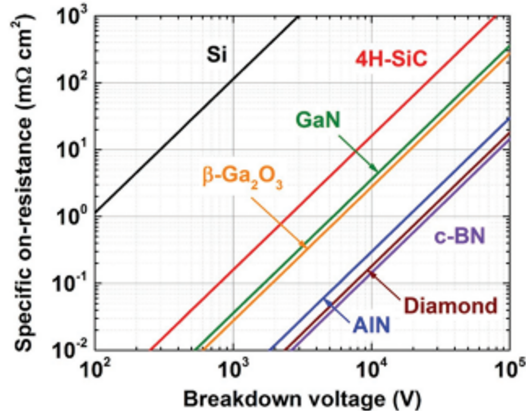


Figure 2.5 Log-log plot of ON-resistance versus breakdown voltage, for Si, Sic, GaN, AlN, Ga₂O₃, Diamond and c-BN (cubic Boron Nitride). Figure from [32].

Certain practical and theoretical challenges currently restrict the widespread application UWBG semiconductors in high-power devices. For diamond and AlN, doping presents difficulties due to their large bandgaps. Additionally, AlN substrates (for homoepitaxy) are expensive and not easily obtainable. Heteroepitaxy on GaN substrates is limited to low Al-content. Although Gallium oxide offers the significant advantage of cheap and readily available high-quality native substrates grown from bulk, addressing its low thermal conductivity requires innovative device architectures and processing methods.

2.7 Strain and dislocations

Epitaxy is a process that involves the deposition (growth) of a crystalline layer (epi-layer) on top of a substrate. If the grown layer and the substrate are the same material, the process is termed homoepitaxial. If the layer and substrate material are different from each other, the process is referred to as heteroepitaxial. In such case, there are differences in lattice constants (lattice mismatch) and thermal expansion

coefficients between the two. Lattice mismatch (or misfit) is defined as:

$$f = \frac{a_S - a_L}{a_L} \quad (2.3)$$

where a_S and a_L are the unstrained in-plane lattice constants of the substrate and the layer, respectively.

In the heteroepitaxy of thin epilayers on considerably thicker substrates, and where the lattice mismatch is no greater than a few percent, the epilayer will elastically strain biaxially to adopt the in-plane lattice constant of the substrate, $a_{S,\parallel}$. This is called coherent growth, as no structural lattice defects are formed. If the unstrained in-plane lattice constant of the layer, $a_{L,\parallel}$, is greater than the corresponding lattice constant of the substrate $a_{S,\parallel}$ the in-plane strain will be compressive (Figure 2.6 (left)). If $a_{L,\parallel} < a_{S,\parallel}$, the in-plane strain is tensile (Figure 2.6 (right)). For compressive / tensile strain, the layer will expand / contract vertically to preserve bulk density. Such layers are termed pseudomorphic [38].

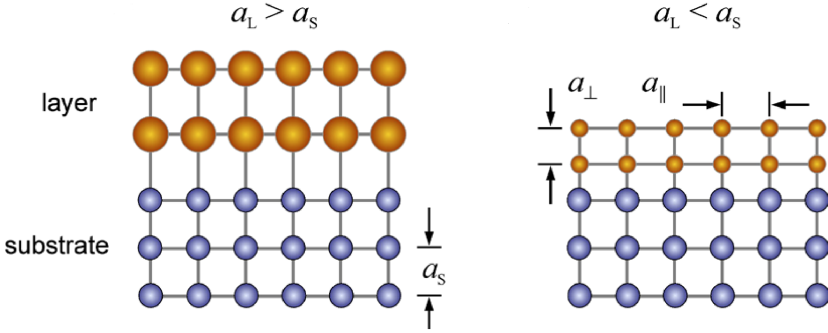


Figure 2.6 Epilayers under compressive in-plane strain (left), and tensile in-plane strain (right). The layers are pseudomorphic, because they are elastically strained. From [39].

Strain energy accumulates as the layer grows thicker, and it does so at a faster rate for higher values of lattice mismatch. There exists a critical layer thickness, which scales inversely with the lattice mismatch, beyond which the strain energy is higher than the formation energy for extended structural irregularities in the crystal lattice. As a result, the crystal relaxes the accumulated strain energy in the layer by a plastic deformation through the introduction of extended defects (dislocations) at the interface between the layer and the substrate. At the end of the process, the layer's lattice constant approaches its natural (unstrained) value, reducing the misfit. In such a way the Gibbs free energy at the interface, which is the sum of the stored strain energy and the formation energy of the dislocation, is minimized.

Dislocations represent one-dimensional (1-D) or line defects. Dislocations are described by the line dislocation vector $\vec{\Gamma}$ along which the crystal lattice is disrupted,

and the Burges vector \vec{b} , whose direction and magnitude respectively describe the direction and amount of distortion from an otherwise perfectly periodic lattice. Dislocations for which $\vec{b} \parallel \vec{l}$ are called screw dislocations. (Figure 2.7 right), as they involve spiral distortion in the lattice structure by an amount equal to $|\vec{b}|$. Dislocations for which $\vec{b} \perp \vec{l}$ are called edge dislocations' (Figure 2.7 left) they involve the introduction of a half-plane spanned by $\vec{b} \times \vec{l}$ and \vec{l} . Most dislocations have a mixed character between the two groups, with angles between b and l between 0 and 90 degrees.

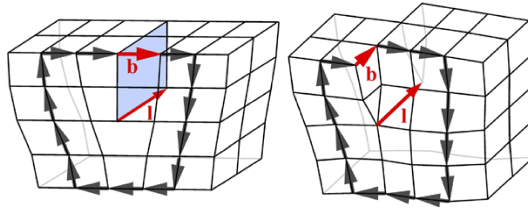


Figure 2.7 Edge (left) and screw (right) dislocations. From [39]

Dislocations can form closed loops or clusters within the crystal, terminate at grain boundaries (two-dimensional arrays of dislocations), merge and / or annihilate with another dislocation, or penetrate and terminate at the surface giving the appearance of pits in atomic force microscopy (AFM) images.

A variety of models have been developed to estimate the critical thickness for plastic deformation in strained wurtzite-type epilayers, that minimises the total energy at the interface. A commonly accepted model is that of Fischer et al. [40], which for AlGaN-on-GaN predicts the behaviour shown in Figure 2.8 for the critical thickness as a function of Al composition, x . The critical thickness decreases with increasing Al content, due to the increase in tensile strain. Growth beyond critical thickness without application of appropriate strain management strategies would lead to cracks in AlGaN.

Dislocations in epilayers are undesired as they perturb the lattice potential, thereby serve as scattering or trap centers for carriers, affecting the mobility of carriers and offering paths for current leakage that degrade device performance [5]. One potential mechanism for the leakage currents below the breakdown voltage involves the hopping of carriers between dislocation traps [42]. The dangling bonds along the dislocation lengths introduce deep states within the bandgap, which deteriorate the physical performance of the crystal. The strain field around their cores can attract point defects; thereby they can act as nucleation sites for precipitates of dopant atoms activated by thermal energy during growth or device processing, inducing local inhomogeneities in material properties. Hence, minimizing dislocations and achieving crack-free epitaxial layers are particularly important for their implemen-

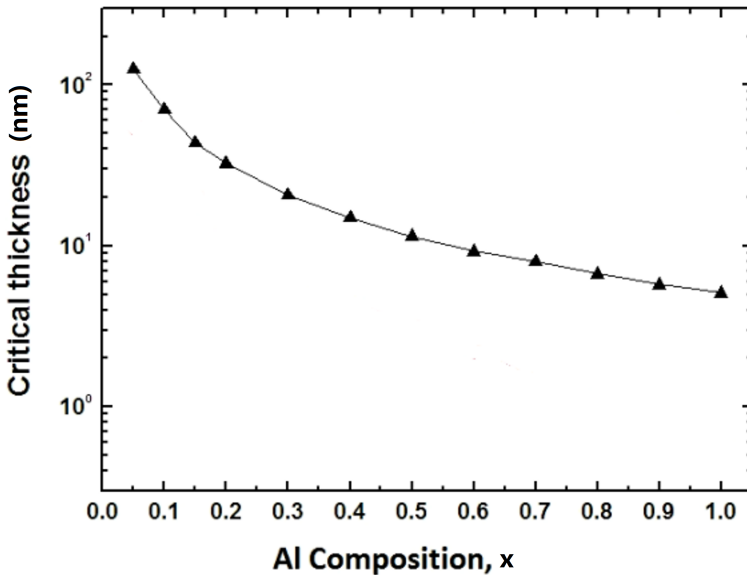


Figure 2.8 Critical thickness for plastic relaxation in AlGaIn, plotted versus Al content, x . Calculated in [41] for dislocations with a 60° angle between the Burgers and line dislocation vectors.

tation in electronic devices.

Reduction of threading dislocation density (TDD) in heteroepitaxial layers can be achieved by the introduction of a relatively thick layer between the epilayer and substrate, of the same lattice constant and thermal expansion coefficient as the epilayer, the so-called buffer layer. As a result of the lattice mismatch, this buffer layer will plastically relax and adopt its unstrained lattice constant. This allows for the growth of nearly dislocation-free and crack-free epilayers on top, as dislocations are restricted and annihilate within the volume of the thick buffer, inhibiting the penetration of threading dislocations to the active part of the device. This method has the advantage that the TDD reaching the epilayer decreases inversely with buffer thickness; however impractically thick micrometer-sized buffers are generally needed to sufficiently decrease the TDD [39]. Another method involves the growth of a compositionally graded buffer; that is, an alloy where the value of the lattice constant is changed continuously or in a stepwise manner by tuning the alloy parameters from the lattice constant of the substrate below the buffer to the value of the lattice constant of the epilayer above. For instance, for the growth of thick drift layer of $\text{Al}_{0.06}\text{Ga}_{0.94}\text{N}$ – on – GaN , the gradation can be achieved step-wise by tuning the Al molar fraction from a lower value at the interface with the substrate, to a value of 0.06 at the interface with $\text{Al}_{0.06}\text{Ga}_{0.94}\text{N}$. As a result, it is possible to limit the accumulation of tensile strain energy at each interface to values that are generally lower

than the formation energy for dislocations or crack propagation. This is achieved due to the lower mismatch between neighboring layers in a single step, as compared to the mismatch between AlGaN and substrate, resulting in generally lower dislocation density. The dislocations that are formed bend at each interface in the grading, annihilating as they meet. This method promises to enable the growth of crack-free AlGaN with low dislocation density beyond the critical thickness. However, achieving it requires simultaneous optimization of various variables; including the total buffer thickness, the number of grading steps, the doping of the buffer, and the step size relative to the total buffer thickness. Certain studies have indicated that thicker graded buffers for a fixed number of steping layers may not always be beneficial. Contrary to intuition, increasing the number of steps for a given buffer thickness does not necessarily lead to improved results either [43]. The strain relaxation efficiency of the graded buffers is also known to depend on the growth temperature and growth rate [44].

Buffer layers aim to address another critical issue related to the thermal mismatch, which is often calculated in terms of percentages as $[(\alpha_L - \alpha_S)/\alpha_L] \times 100$, where $\alpha_L - \alpha_S$ is the difference in coefficients of thermal expansion (CTE) between the layer and substrate. As temperature is varied, to first order the lattice constant of crystals obeys the following relation:

$$a(T) = a(T_0)[1 + \alpha(T - T_0)] \quad (2.4)$$

where T_0 is the initial temperature. Large thermal mismatches between layers and/or substrate can lead to the accumulation of significant amount of strain energy during cooling to room temperature after epitaxy. In case of tensile strain, this can lead to cracks in epitaxial layers. CTEs are complicated functions of temperature as seen in Figure 2.9 for GaN and AlN. This suggests that the minimization of dislocation densities requires appropriate post-growth cooling rates.

2.8 Substrates for GaN homo- and hetero-epitaxy

If the substrate used for epitaxy is non-native (foreign) to the layers, as in heteroepitaxy, additional layers are needed for strain accommodation. At each interface between the additional layers, extended defects can occur due to the lattice and CTE mismatch. Homoepitaxy offers the best route to avoiding the formation of dislocation microstructures that appear in heteroepitaxy. The ideal substrates in epitaxy should be a) high quality, b) perfectly (or nearly) structurally and thermally matched with the epilayer, and c) cheap. In addition, substrates are typically miscut across their epi-surface, by about a tenth of a degree, in order to promote step-flow growth – which enables higher growth rates for a certain supersaturation, as well as uniform alloying and dopant incorporation. Therefore, in order to ensure lateral uniformity in the off-cut across the substrate, it is desirable for the ideal substrates to also have minimal bowing.

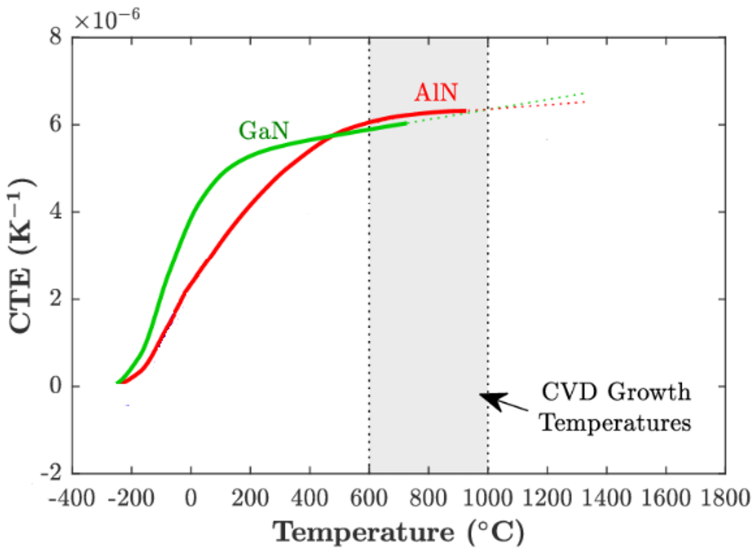


Figure 2.9 Temperature dependence of the CTE for GaN and AlN. Adapted from [45].

However, GaN crystal growth from melt (as in liquid phase epitaxy) requires extreme conditions, because of: i) the high equilibrium partial pressure of Nitrogen (60kbar) at the high melting temperature of GaN (2200°C) and ii) for temperatures below 2200°C, N dissociates from GaN (incongruent evaporation). Similar difficulties are encountered for the growth of AlN ingots from melt. For the growth of III-nitride substrates therefore, vapour phase and solution-based growth methods have been developed. Halide Vapor Phase Epitaxy (HVPE) and amonothermal methods for the growth of GaN substrates are still limited to the production of small wafer sizes compared to Silicon, with higher defect and dislocation density than Si wafers and substantial cost. As a result, the epitaxy of GaN has typically been performed on foreign substrates, such as Si, SiC or Sapphire (Al_2O_3).

Heteroepitaxy of GaN on SiC substrates offers lower defect densities than on sapphire and Si substrates, due to the lower lattice mismatch (Table 2.3), but it is much more expensive by comparison. The higher thermal conductivity of SiC provides better thermal dissipation for power devices as well, but SiC is much more expensive by comparison. GaN on sapphire (001) experiences considerable compressive strain due to the higher thermal and lattice mismatch, resulting in higher edge and screw dislocation densities, wafer bowing and rougher surface morphology. In addition, GaN-on-sapphire is not a good choice for power electronics due to the comparatively low thermal conductivity. Si and sapphire are similarly structurally mismatched to GaN, but Si substantially more thermally mismatched. Due to the the larger lattice constant of Si (111) compared to GaN (0001), GaN-on-Si is typically already tensely strained at growth temperature. The larger CTE of GaN relative to

Table 2.3 Material properties of commonly employed substrates for GaN epitaxy: Si, SiC, Sapphire and GaN.

	Si	SiC[34][46]	Sapphire	GaN
In-plane lattice constant at 300K (Å)	5.431	3.080	4.765 [32]	3.189
In-plane CTE (10^{-6}K^{-1})	2.4 [8]	3.3	5.0 [8]	5.6 [8]
In-plane lattice mismatch	-70% (on (111) Si)	3.4%	-49%	0*
In-plane CTE mismatch	57%	41%	11%	0
GaN epilayer dislocation density (cm^{-2})	$\approx 10^9$ [8]	$\approx 5 \times 10^8$ [9]	$\approx 10^9$ [8]	$10^4 - 10^6$ [32]

* GaN substrates used here are fabricated by HVPE method, which is based on heteroepitaxy and subsequent removal of the substrate to produce the quasi-bulk GaN material. Hence, a small difference from relaxed (ideal) GaN lattice constants is expected.

Si stipulates further additional the strain during cool-down to room temperature, resulting the formation of multiple cracks.

For the growth of high-quality AlGaIn drift layers for vertical power devices, GaN substrates are a good choice for low Al contents. For higher Al contents, AlN substrates are ideal, as the strain is compressive instead of tensile, avoiding the formation of cracks. GaN homoepitaxy on bulk GaN substrates produces epitaxial layers of the lowest dislocation density. Free-standing AlN and GaN substrates are currently very expensive, however.

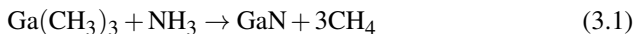
3

MOVPE

3.1 General concepts

MOVPE has become the method of choice for the epitaxial growth of group-III nitride based materials and device structures. It is the most versatile epitaxial technique. Its major advantages include reproducible high quality growth of uniform epitaxial layers with very low concentration of impurities, at high growth rates and yields. In-situ monitoring systems allow for monitoring and the optimisation of the growth process.

In MOVPE reactors crystalline growth is realized via the decomposition through the chemical reactions of the gas-phase precursors (source compounds) at the surface of the substrate where the elements for growth are released. The precursors involved in the reaction can be hydrides (such as silane or arsine) and volatile molecules in metal-organic form MR_n , where M is the source metal element and R_n alkyl radicals such as (methyl or ethyl) which serve as organic ligands. For the MOVPE growth of GaN, the overall reaction typically involves the metal-organic (MO) precursor trimethylgallium (TMGa) and ammonia.



A coherent account of the overall MOVPE growth process involves the description of a variety of interconnected processes, each of which controls certain aspects of the growth process. Thermodynamics defines the maximum driving force for the growth, while hydrodynamics (mass transport) determines the diffusion rate of the precursors to the vapour / solid interface. Kinetics controls the rates of the processes that occur at the surface, such as chemical reactions and diffusion rates. The latter two will also depend on the chemistry of the precursor molecules used, and on the details of the surface – such as its orientation and reconstruction. The MOVPE growth process is also highly sensitive to the reactor hardware and configuration, as well as to the growth conditions, defined by variables such as temperature, reactor pressure and V / III ratio.

Figure 3.1 illustrates a simplified description of the steps that occur during the MOVPE growth process of GaN. The metal organic precursor TMGa and ammonia are carried to the reactor by the carrier gases H_2 and N_2 – the driving force being the pressure difference between the inlet (high-pressure region) and outlet (low-

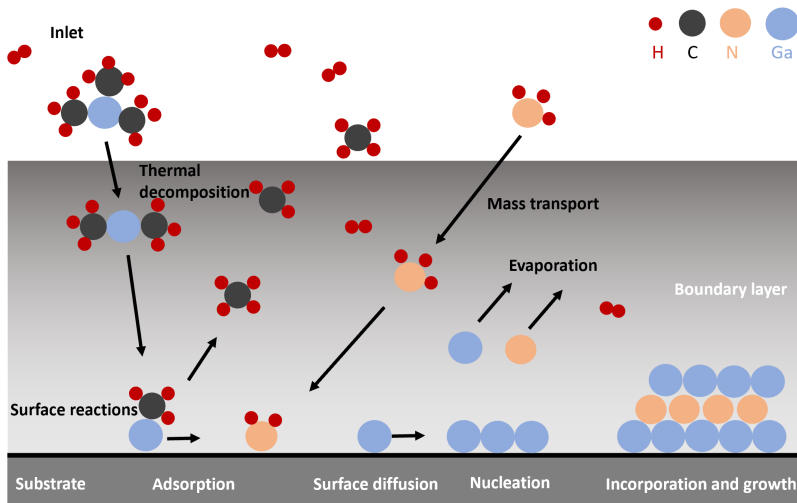


Figure 3.1 Simplified schematic description of the steps that occur during the MOVPE growth process of GaN.

pressure region). Next, the precursors diffuse vertically from the high concentration at the inlet down to the lower concentration at the substrate, ideally under laminar flow to ensure uniformity in growth rate. At the surface, they thermally decompose and undergo surface chemical reactions, releasing active species (adatoms) which adsorb on the substrate. The adsorbed species diffuse laterally across the substrate until they either nucleate, or are incorporated into an atomic step, to a stable nucleus, or to suitable crystal sites (such as kink sites); resulting in growth of GaN solid. Evaporation of the MO species from the substrate is also possible at higher temperatures. The latter, together with the gas-phase by-products of precursor decomposition and surface reactions are pumped out of the system through the exhaust pump.

The gradient in MO precursor concentration between the inlet and substrate where they are consumed, is generally smoothed out within a stagnant boundary layer, with strong consequences for the MOVPE growth process. Figure 3.2 illustrates the velocity profile of a laminar and isothermal flow of a gas near a flat substrate. The combined effect of frictional forces from the reactor walls and substrate on the MO precursor molecules serve to slow down the diffusion process and hence the gas velocity component u_x decreases from its the free-stream gas velocity u_0 down to zero at the substrate. This region defines the boundary layer. The gradient in concentration and hence the diffusion rate to the substrate decreases with the thickness of the boundary layer, limiting the growth rate. The boundary layer thickness increases with the viscosity ν of the MO precursor gas and distance x traveled across

the substrate according to the following proportionality relation

$$\delta(x) \propto \sqrt{\frac{\nu}{u_0} x} \quad (3.2)$$

It follows that the use of H_2 as a carrier gas allows for a higher growth rate due to its lower viscosity relative to N_2 . A higher reactor pressure has the opposite effect, as it decreases the laminar gas velocity, leading to a thicker boundary layer - and to a slower growth rate as a result - and less Carbon incorporation [13]. The boundary layer becomes thinner with increasing gas flow rates.

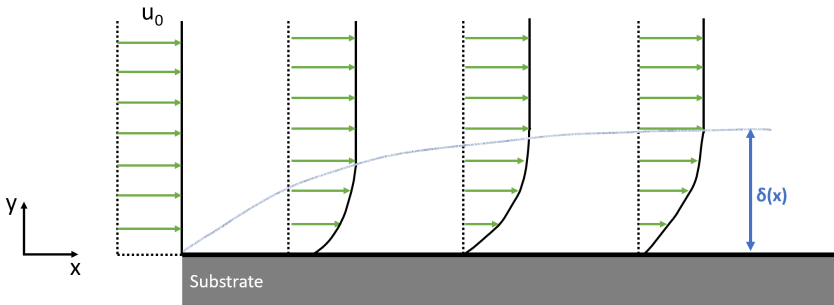


Figure 3.2 Schematic representation of a boundary layer with thickness δ forming above the surface of a flat thin plate under a laminar gas flow.

3.2 Growth regimes

The growth rate is determined by the slowest of the steps described above. Process steps such as evaporation, mass transport and kinetics are temperature dependent. This results in three main growth regimes as a function of growth temperature T_g , as illustrated in the log-log plot in Figure 3.3.

Kinetically- or reaction-limited growth regime. In this regime, the supply rate of precursors from the gas-phase to the vapour-solid interface is well above the growth reaction rates. At relatively low growth temperatures T_g there is insufficient thermal energy for thermally-activated processes, such as precursor decomposition, surface diffusion and chemical reactions. The growth rate, therefore, is limited by reaction kinetics and follows an Arrhenius dependence on temperature. MOVPE is generally not conducted in this regime because the growth rate is highly sensitive to temperature, making it challenging to achieve the desired control.

Transport- or diffusion-limited regime. At higher growth temperatures there is sufficient thermal energy for fast kinetics, but the diffusion of the gas-phase precursors (mass transport) through the stagnant boundary layer to the vapour-solid interface

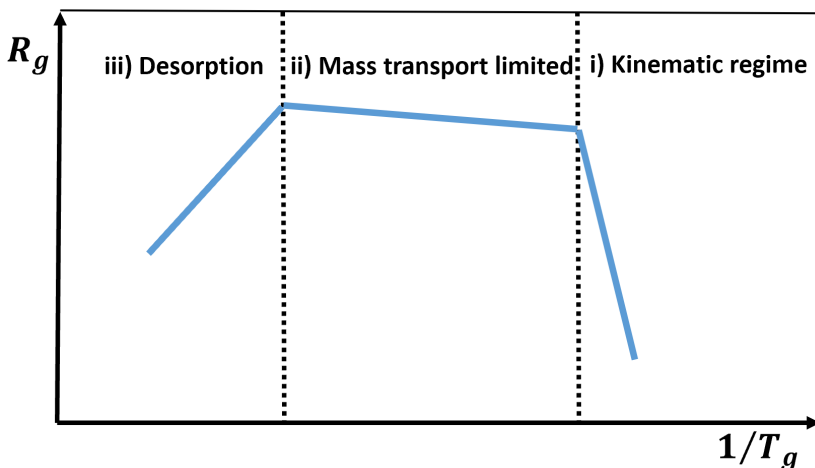


Figure 3.3 Temperature dependence of the growth rate, R_g where the three main growth regimes are indicated.

is the limiting factor for the growth rate of epilayers. In the growth of III-nitrides, typically ammonia is oversupplied as it is substantially more volatile than group-III precursors. In other words, V / III ratios of the order of a thousand are used. To achieve stoichiometric growth of GaN however, equal numbers of Gallium and Nitrogen atoms are extracted from the gas-phase precursors [47]. As a combined result, the partial pressure of ammonia at the interface, will not drop much from its value at the source, but the partial pressure of TMGa will experience a sharp drop depending on the incorporation rate of Ga into the solid. As a result, the growth rate in the mass transport regime is mainly controlled by the input partial pressure of Ga, the diffusivity of group-III precursor through the boundary layer and on the thickness of the latter. The linear dependence of the flux of group-III precursors arriving at the interface – and hence of the growth rate - on the input partial pressure of TMGa is quite convenient for MOVPE, as the latter can be easily controlled through the flow rate of TMGa into the reactor. This is one of the main reasons why MOVPE growth of planar layers is performed at this growth regime. In addition, the weak temperature dependence of the growth rate in this regime is convenient for controlled growth of planar layers with uniform doping level, alloy composition and smooth surface morphology. The growth rate in the mass transport regime can be increased by reducing the reactor pressure P_{tot} , as this diminishes both the diffusion constant and the thickness of the boundary layer, allowing for larger flux of precursors to the interface – but at the expense of higher unintentional Carbon incorporation [13].

Desorption regime. At higher growth temperatures, there is sufficient thermal energy for the adatoms to overcome the desorption barrier and evaporate / desorb

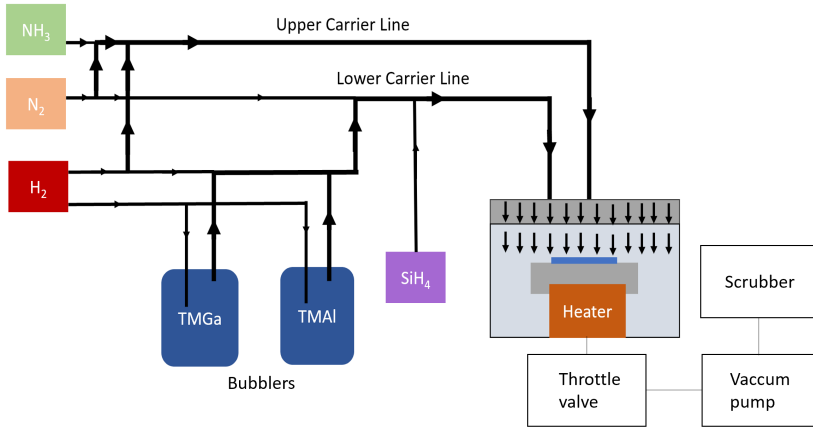


Figure 3.4 Simplified schematic of a MOVPE system.

from the surface, leading to layer decomposition. In addition, very high temperatures promote gas phase reactions and deposition on reactor sidewalls, which reduce the available active reactant species at the interface. As a result, in the desorption regime, the growth rate decreases with increasing temperature.

3.3 Close-coupled showerhead (CCS) MOVPE system

Figure 3.4 depicts a simplified schematic of a close-coupled showerhead (CCS) MOVPE system. The left side of the diagram depicts the gas blending system which controls the flow and the mixing of the carrier gases (N_2 and H_2), Group-III precursor and hydride gases. The flows are enabled by the switching of electronically-controlled valves, and quantified through mass-flow controllers (MFC) in units of cubic centimeters per minute (ccm). MO precursors and ammonia gas are transported to the reactor via two different carrier lines, to avoid their pre-reaction. Substrates for growth are placed in sunken pockets of a substrate carrier called susceptor, which is made of SiC-coated graphite and is resistively heated up to growth temperature. Reactor pressure P_{tot} is controlled by the throttle valve at the end of the reactor, while unreacted and unused by-products of chemical reactions are filtered out in a scrubbing system.

MO precursors are stored in liquid baths - bubblers - at highly-controlled ambient temperature to ensure a well-defined precursor equilibrium vapour pressure, given in units of mbar by

$$P_{eq,MO} = 10^{a-b/T} \quad (3.3)$$

where T is the storage temperature in the liquid in units of Kelvin, and a and b are parameter with values 8.07 and 1703 K respectively for TMGa, and 8.22 and 2134 K

respectively for TMA. The bubbler storage temperatures of TMGa and TMAI were in the range 4-10 Celsius and 14-20 Celsius, respectively. To initiate a flow of MO precursors out of the bubblers, a flow Q_{MO} (in ccm) of carrier gas is injected into the thermal bath, creating liquid bubbles enriched in MO molecules. The resulting bubbler pressure P_B is read by a pressure controlled at the outlet port of the bubbler. This serves to extract an actual precursor flow given in units of ccm by $Q_{a,MO} = \frac{Q_{MO}P_{eq,MO}}{P_B - P_{eq,MO}}$. The input partial pressure of the MO precursors can be estimated from the relation

$$P_{MO} = P_{tot} \frac{Q_{a,MO}}{Q_{tot}}, \quad (3.4)$$

where Q_{tot} the cumulative sum of Q_{MO} flows, ammonia and carrier gas flows, in units of ccm. The bubbler pressures for TMGa and TMAI were in the range 1750-1950 mbar and 1250-1500 mbar, respectively. Another flow of carrier gas – called *push flow* – is introduced into the bubbler containers to enhance the extraction efficiency of the vaporised precursors, with no effect on their input partial pressures.

Precursor molar flows can be estimated from the ccm flows from the following equation:

$$\chi_{MO} = \frac{Q_{MO}P_{eq,MO}}{P_B - P_{eq,MO}} \frac{1}{22.4l/mol} \frac{1}{1000cc/l} \quad (3.5)$$

where 22.4 l/mol is the molar volume in the ideal gas approximation.

The input partial pressure of ammonia is given by $P_{NH_3} = \frac{Q_{NH_3}}{Q_{tot}} P_{tot}$, and the V/III ratio can be estimated by $\frac{P_V}{P_{III}} = \frac{Q_{NH_3}}{Q_{a,MO}}$.

Silane (SiH_4) serves as the Si precursor in our MOVPE process. Its flow rate depends on 4 factors: i) the MFC source flow rate, s , ii) the flow rate of the diluting H_2 gas, d , iii) the flow rate of the diluted silane in the reactor, inj and iv) the fraction of Si in the silane gas container (10^{-4}):

$$Q_{SiH_4}(ccm) = \left(\frac{s}{s+d} \times (inj) \times 10^{-4} \right) \quad (3.6)$$

The expected intentional Si concentration in GaN can therefore be estimated by $[Si] = \frac{Q_{SiH_4}}{\sum_i Q_{a,MO,i}} \times 4.45 \times 10^{22} cm^{-3}$ where 4.45×10^{22} is the number of Ga sites available for Si incorporation, per cubic centimetre. The latter is estimated from $6/(1.5\sqrt{3}a^2c)$, where a and c are the relaxed GaN lattice parameters, and 6 is the number of Ga atoms in the wurtzite unit cell. The actual and intentional n-type doping concentration will depend on the Si incorporation on Ga sites, and the compensation due to vacancies and background impurities.

Figure 3.5 illustrates the CSS reactor in cross-section. In the CSS reactor, the precursor and carrier gases are introduced through a collection of narrow (circa 0.5mm)

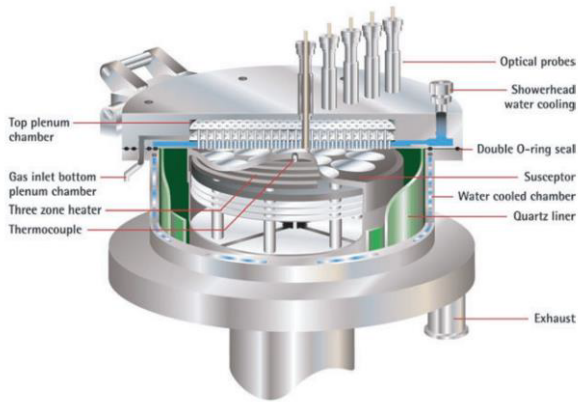


Figure 3.5 Growth chamber for a CCS MOCVD reactor. From [48].

tubes arranged vertically on top of the reactor, which forms the *showerhead*. To prevent pre-reactions between ammonia and MO precursors, the two gases are fed into the reactor via two different compartment of tubes in the showerhead – called the group-III (top) and Group-V (bottom) plenums. Each group-V tube is surrounded by four group-III tubes, and conversely, for effective mixing of the reactants.

A tungsten-based heater situated below the susceptor and comprised of several heating zones heats the susceptor. For a uniform temperature distribution across the entire susceptor (to within 1°C) the heater zone located at the edge receives the highest power input to compensate for the radial gradient in heat dissipation across the susceptor. Thermal radiation emitted below the heater is reflected back towards the susceptor by molybdenum plates located below the heater. The temperature of the susceptor is read by a thermocouple located under it. The susceptor is supported on a quartz structure, and rotates at an appropriate angular velocity for a uniform supply of precursors across its area and to decrease the boundary layer thickness [49]. The reactor is *cold-wall* since a cooling water flow is fed to the sidewalls of its chamber via a tube. To prevent premature thermal decomposition of the reactant gases, a second flow of cooling water (circa 50°C) is provided through a tube below the group-V compartment. The thicker tubes on top of the showerhead serve as ports for the in-situ monitoring systems.

The CCS reactor is *close coupled* since the showerhead and susceptor are in close proximity; separated by a vertical gap of about 11 mm. Small susceptor-showerhead gaps provide for a thinner and uniform boundary layer thickness – and hence for a faster and uniform growth rate - across the susceptor. The deposition of precursor gases on the substrate is enhanced, and parasitic gas-phase reactions are reduced thanks to the short gas-phase transport distance; further benefiting the growth rate. Smaller gaps than about 11 mm give rise to non-uniform flow distributions across the susceptor, leading to unwanted thickness variations in the grown epilayers, as

well as to premature thermal decomposition of the reactant gases within the showerhead compartments [49].

The thicker tubes on the showerhead lid serve as ports for the in-situ monitoring system. Laser light from the interferometer is shone vertically down the substrate through three different ports, and the reflected light collected by a photodetector. As a planar epilayer is grown on a substrate, conditions for constructive interference are fulfilled at each instance when the optical path difference between the rays reflected from its upper and lower interfaces equals an integer multiple of the wavelength λ of the light. This gives rise to Fabry-Perot reflectance oscillations [50]. Assuming normal incidence, for a growth time interval Δt peaks in reflectance occur when $2d_i = m\lambda/n_1$ and $2d_f = (m+1)\lambda/n_1$, where n_1 is the (temperature-dependent) refractive index of the layer, and d_i and d_f respectively the initial and final thickness of the layer. We assume that $n_1 = 2.4$ for GaN. The growth rate can be extracted from $R_g = (d_f - d_i)/\Delta t = \lambda/2n_1\Delta t$. To monitor the growth of GaN epilayers, laser light of $\lambda = 632\text{nm}$ is used. The amplitude of the Fabry-Perot oscillations can be used to obtain information on the surface morphology of the epilayers. Rough and/or wavy surfaces diminish the amplitudes of the reflectance peaks, due to the randomized optical path differences and scattering inside the layer.

As an example, Figure 3.6 provides the complete reflectance curve obtained using 632 nm laser light for the AlGaIn₃-on-GaN sample (explained in Section 5). The first reflection peak occurs as the temperature is increased up to 980°C, and probably represent the formation of a gallium oxynitride layer, since during this time only ammonia and hydrogen carrier gas is flown into the reactor. As temperature is increased up to growth temperature, 1040°C, a roughening of the surface is suggested by the decrease in reflectance intensity during this time. Periodic oscillations in the reflectance curve become apparent once the reactor temperature reaches the growth temperature (1040°C) and the TMGa flow is initiated. Within the labeled region 1, for instance, it is possible to fit 2.44 Fabry-Perot periods, indicating a film growth of 324 nm (calculated as $\lambda \times 2.44/2n_1$). The amplitude of the reflectance peaks within the three labelled regions gradually decreases as the layer thickness increases, owing to the wavy morphology of GaN-on-GaN baselines that diminishes the coherence of the reflected light. Wavy surfaces here refer to surfaces with features much larger than the laser wavelength, whereas 'rough' surfaces possess features comparable to the laser wavelength. The scattering from rough surfaces exacerbates the decline in light coherence, leading to reductions in both the amplitude and intensity of the reflected curves as the growth progresses.

During the course of this work, difficulties were encountered in obtaining sufficient reflectance intensity from GaN-on-GaN and AlGaIn₃-on-GaN samples, perhaps due to their small size. As a result, in order to monitor the growth, and estimate the thicknesses of the grown epilayers, each growth run on a GaN substrate was performed in parallel with the same growth on a GaN-template. Due to data protection concerns,

3.3 Close-coupled showerhead (CCS) MOVPE system

extracting the in-situ reflectance measurement data from the company's computer was also difficult. Therefore, this data is not presented further in this study.

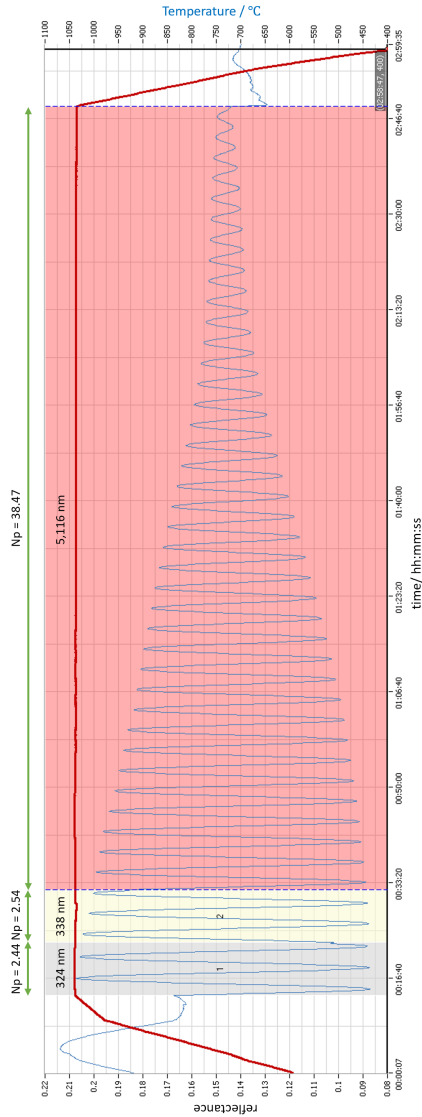


Figure 3.6 In-situ reflectance curve for AlGaIn₃ (light blue), and growth temperature (red), plotted as reflectance intensity as a function of time.

4

Characterization methods

4.1 X-ray diffraction

X-ray diffraction is a non-destructive method for the assessment of the structural quality of epitaxial layers. It allows for the extraction of crystallographic information such as material crystal structure and lattice constants, the quantification of strain and density of dislocations present in the epilayers, as well as alloy compositions.

4.1.1 Basic concepts

Electrons in materials scatter X-ray beams and have a (Thomson) scattering cross-section of about 0.665 barn ($6.65 \times 10^{-29} \text{m}^{-2}$) [51]. In classical terms, the oscillating electric field component of the incoming X-ray beam accelerates the charges leading to Thomson scattering, which presents the elastically scattered waves. A crystal can be thought of as a periodic arrangement of coherent scatterers. As a result, the scattered light may undergo constructive or destructive interference, since it is a superposition of scatterings from individual electronic volume elements. To assess this superposition, the phase difference between the incident and scattered beams at each volume element must be considered.

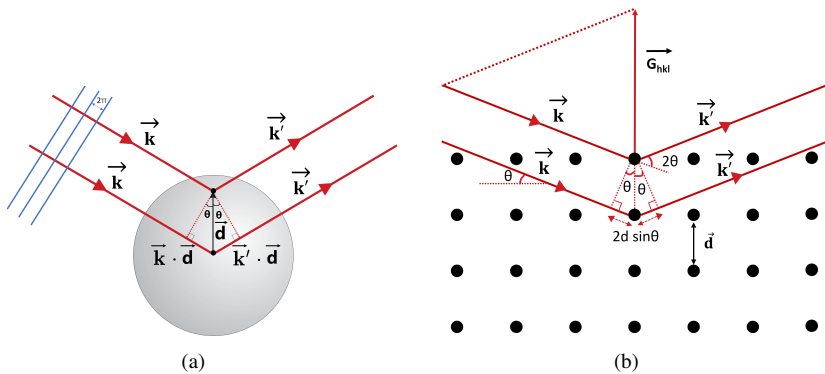


Figure 4.1 (a) Scattering from two electrons in the far-field approximation [52]. (b) Diffraction from parallel planes spaced by a distance d .

Figure 4.1 (a) shows a hypothetical atom with 2 charges separated by a distance d , illuminated by a monochromatic X-ray beam with wavevector $\vec{k} = \frac{2\pi}{\lambda} \vec{n}$ - where \vec{n} is unit vector in the direction of \vec{k} - and assumes that the source and detector are sufficiently separated for a plane-wave representation of the scattered and incident X-rays. The phase difference of the incident and scattered beams between the two charges is $\Phi = (\vec{k}' - \vec{k}) \cdot \vec{d}$, while the condition for constructive interference $\Phi = (\vec{k}' - \vec{k}) \cdot \vec{d} = 2\pi n$, where n is an integer.

Each lattice point in a perfectly periodic 3D crystal lattice can be defined by the vector $\vec{R}_n = n_1 \vec{a}_1 + n_2 \vec{a}_2 + n_3 \vec{a}_3$ where \vec{a}_j are basis vectors for the periodically repeating motif (unit cell) in the structure and n_j are integers. Since the condition for constructive interference holds for all possible \vec{d} , in a crystal it can be generalized to $(\vec{k}' - \vec{k}) \cdot \vec{R}_n = 2\pi n$, or equivalently to $e^{i(\vec{k}' - \vec{k}) \cdot \vec{R}_n} = 1$. It is fulfilled when $(\vec{k}' - \vec{k})$ defines another lattice, reciprocally related to the direct lattice determined by \vec{R}_n and defined by vector $\vec{G}_{hkl} = h\vec{a}_1^* + k\vec{a}_2^* + l\vec{a}_3^*$, where h, k, l are integers (Miller indices) and \vec{a}_j^* are the reciprocal lattice vectors. The latter are reciprocally related to the corresponding direct lattice vectors; $\vec{a}_j^* \cdot \vec{a}_j = 2\pi \delta_{ij}$, where δ_{ij} is the Kronecker delta. A non-vanishing scattering intensity from a perfect crystal occurs only when the change in wavevector $(\vec{k}' - \vec{k})$ is a reciprocal lattice vector \vec{G}_{hkl} . This statement defines the Laue's condition for diffraction, $(\vec{k}' - \vec{k}) = \vec{G}_{hkl}$. The condition $e^{i\vec{G}_{hkl} \cdot \vec{R}_n} = 1$ describes an infinite set of parallel planes - (hkl) planes - that contain all the direct lattice points, perpendicular to \vec{G}_{hkl} , and spaced by $d_{hkl} = 2\pi n / |\vec{G}_{hkl}|$ (Figure 4.1 (b)). Since $|\vec{G}_{hkl}| = 2k \sin \theta$, where θ is the angle the incoming and diffracted beams make with the horizontal plane, this leads to Bragg's condition for diffraction:

$$n\lambda = 2d \sin \theta \quad (4.1)$$

Therefore, as a consequence of crystalline long-range order, diffraction peaks will be observed at the angles θ at which Laue's or Bragg's conditions for diffraction are fulfilled, as a result of constructive interference from (hkl) planes. In this context, n is the ratio of $|\vec{G}_{hkl}|$ to the shortest reciprocal lattice vector parallel to it.

4.1.2 Experimental setup and measurement modes

For the structural characterization of the samples in this thesis, a PANalytical high-resolution X-ray diffractometer (HR-XRD) was used. HRXRD instruments integrate a monochromator to the incident beam path, and an analyzer crystal to the diffracted beam path, to respectively reduce the angular divergence and bandwidth of the beam. The source and monochromator provided X-ray radiation with $\text{CuK}\alpha_1$ line $\lambda = 0.15405974$ nm. In combination with the analyser and detector, fast mea-

measurements of θ at a resolution of about 11 arcsec could be achieved. Fig 4.2 (a) illustrates the basic measurement geometry and the relevant angles.

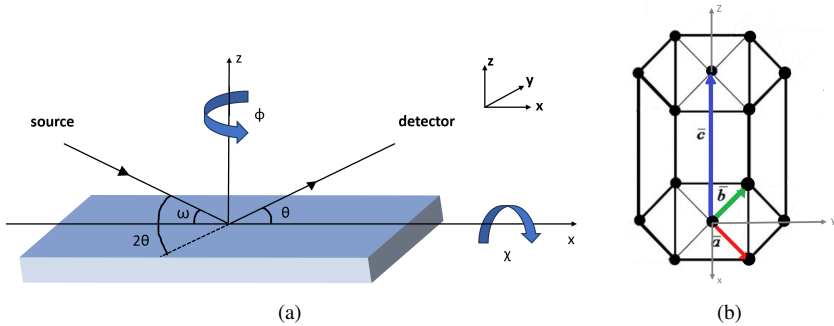


Figure 4.2 (a) Schematic illustration of the measurement geometry and the relevant angles. (b) Schematic of the wurtzite unit cell.

Phi (ϕ) is the rotation angle about the normal to the sample, χ (chi) the clockwise angle between the reciprocal lattice vector of the planes of interest and the substrate normal, while ω is the angle between the incident beam and the sample surface when $\chi = 0$. The angle that the incoming and diffracted beams make with the relevant planes (hkl) that satisfy Bragg's condition for diffraction is the Bragg angle θ , while 2θ is the angle between the incident and the diffracted beams. Both θ and ω lie in the x-z plane.

For hexagonal crystal lattices the notation (hkil) is traditionally used for Bragg planes, where $i = -(h + k)$. Three main types of diffraction geometries include:

a) *Symmetric geometry*. Here, $\omega = \theta$, and $\chi = 0^\circ$ (i.e., \vec{G}_{hkil} is parallel to the normal to the sample's surface). Reflections (hkil) measured in this geometry are called symmetric reflections.

b) *Asymmetric geometry* ($\chi = 0^\circ$, $\omega \neq \theta$). Reflections (hkil) measured in this geometry are called asymmetric reflections.

c) *Skew symmetric geometry*. Here $\chi \neq 0$, as the sample must be tilted by χ to meet diffraction conditions, and $\omega = \theta$. Reflections (hkil) measured in this geometry are called skew symmetric reflections.

Two types of commonly performed scans include:

a) *Rocking curves (RCs)*, in which the relative angle between the source and detector lines is fixed at the angle 2θ that satisfies Bragg's condition for diffraction for a given (hkil) plane, while the sample is oscillated in omega.

b) *$2\theta - \omega$ scans*, in which 2θ is varied by moving both the detector and the source.

These two scans can be performed in any of the three geometries described above.

As will be described in the following section, the full width half maxima of (0002) and $10\bar{1}1$ RCs allow for the estimation of screw and edge (mixed) dislocation densities, respectively. The broadening of the (0002) and $(10\bar{1}1)2\theta - \omega$ peaks on the other hand, relates to the vertical and lateral (mixed) coherence lengths of the mosaic blocks, respectively, as well as to the strain present in the epilayers.

X-rays are absorbed in media. The intensity I of the X-ray beam collected by the detector will be equal to the intensity of the incident beam, I_0 , attenuated by a factor $e^{-2\mu l}$, where $2l$ is the total path length traversed by the beam inside the material (Figure 4.3).

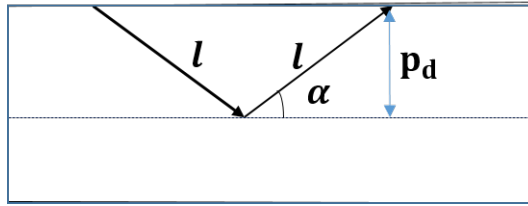


Figure 4.3 Penetration depth p_d as a function of beam-surface angle α and path length l .

The linear attenuation coefficient μ is given by $\alpha \times \rho$, where α and ρ are the wavelength-dependent absorption coefficient and density of the material, respectively. For GaN, their values are about $51.2 \text{ cm}^2/\text{g}$ and $6.15 \text{ g}/\text{cm}^3$, leading to $\mu = 314 \text{ cm}^{-1}$.

The penetration depth, p_d , is often defined as the vertical depth within the material at which the intensity is reduced by half. For reduction by 90% in incident intensity ($I/I_0 = 0.1$) the penetration depth is $p_d = -\sin\alpha \times \ln(0.1)/2\mu$, where α is the angle between the incident beam and the sample surface.

For (0002) reflections measured in a symmetric geometry, $\alpha = \theta^\circ = 17.28^\circ$, hence $p_d = 10 \mu\text{m}$. For $(10\bar{1}1)$ reflections ($\theta = 18.43^\circ$) measured in skew symmetric geometry ($\chi = 61.99^\circ$), $\alpha = \theta \times \cos\chi = 8.66^\circ$, hence $p_d \approx 5.5 \mu\text{m}$.

4.1.3 Estimation of edge and screw threading dislocation densities

In a perfectly periodic, boundless crystal, the diffraction peaks would be delta functions at the angle θ that satisfies Bragg's condition for a given set of (hkl) planes. Dislocations are one of the factors that introduce perturbations to the lattice order, resulting in broadening of the diffraction peaks (due to the less stringent diffraction conditions). Other sources of broadening related to the layers include broadening due to wafer bow, finite size of the crystallites, compositional gradients and strain [53]. In addition, instrumental broadening is also typically present, and becomes more important in low-defect density crystals.

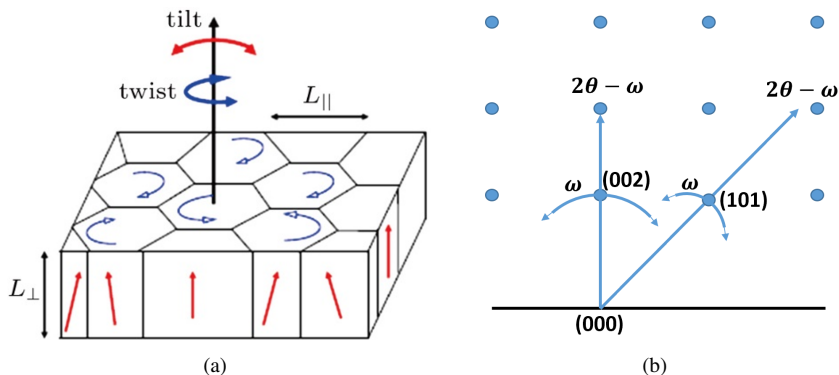


Figure 4.4 (a) Schematic of the mosaicity in a crystal [54]. (b) Schematic of the paths traced in reciprocal space of rocking curves and $2\theta - \omega$ scans, respectively.

Lattice distortions due to dislocations are visualized in terms of the mosaic model [55] which describes the layers as composed of perfect blocks that are tilted relative to the substrate normal and/or twisted about the substrate normal. The X-rays are assumed to scatter coherently within the vertical and lateral dimensions of the mosaic blocks, which are characterised, respectively, by the vertical and lateral coherence lengths. In epitaxy, the vertical and lateral coherence lengths are mainly limited by the edge and screw dislocation densities respectively, as well as alloying; the larger these length, the better the crystal quality. The degree of mosaicity in a crystal is characterised by the breadth of the rocking curves; the higher the mosaicity, the larger the FWHM of the rocking curves, the lower the crystal quality. $2\theta - \omega$ scans trace vertical lines through the origin of reciprocal space to examine the positions of various diffraction spots, and their FWHM relates to the vertical coherence length; the longer the mosaic blocks, the narrower the $2\theta - \omega$ FWHMs. Rocking curves on the other hand trace an arc in reciprocal space around a given diffraction spot in order to quantify the broadening – e.g., due to tilt - that dislocations and the finite coherence lengths introduce (Figure 4.4 b). Screw dislocations have Burgers vector along the c-axis and hence they distort the lattice about the $\langle 0001 \rangle$ direction, which can be characterised by a tilt of the mosaic blocks relative to the substrate normal. The tilt angle and the accompanying broadening of the (0001) peaks become more pronounced as the order n of diffraction peak – and hence the length of \vec{G}_{hkil} – increases. The broadening due to the lateral coherence length of the blocks is independent of the order of diffraction. This allows for the estimation of the tilt angle α_{tilt} through a linear fit for the slope of the data-plot $\beta\omega\sin\theta / \lambda$ versus $\sin\theta / \lambda$, where $\beta\omega$ is the full width at half maximum (FWHM) of the (0002), (0004) and (0006) rocking curves and θ the position of their centres. From the y-intercept in such a plot, the lateral coherence length can be extracted.

The density of threading screw dislocation can be estimated using the following

relation, derived by Dunn and Koch [56] where they assume random distribution of dislocations in the crystal

$$N_s = \frac{\alpha_{\text{tilt}}^2}{4.35 |\vec{\mathbf{b}}_c|} \quad (4.2)$$

and where $|\vec{\mathbf{b}}_c| = 5.1850 \text{ \AA}$ is the magnitude of the Burgers vector along the c-axis. Edge dislocations have Burgers vector parallel to the (0001) planes, hence they do not contribute to the overall tilt about the $\langle 0001 \rangle$ direction.

Edge threading dislocations have Burgers vector along the $\langle 11\bar{2}0 \rangle$. As a result, they induce a twist angle (α_{twist}) of individual mosaic blocks about the substrate normal, and therefore contribute to the FWHM of the asymmetric rocking curves. To estimate this contribution (and hence α_{twist}), rocking curve measurements of asymmetric peaks at inclination angles χ of 90° are needed to filter out any tilt components in peak broadening. In practice, rocking curves at $\chi = 90^\circ$ require edge geometry, bulk or very thick layers, and hence are difficult to perform.

The twist angle α_{twist} can be extrapolated by using the empirical method of Srikant et al [57]. The contributions to the FWHM of the peaks from the tilt and twist components as a function of χ are given by

$$W_0^{\text{tilt}}[\chi] = \cos^{-1}[\cos^2(\chi)\cos(W_y) + \sin^2(\chi)] \quad (4.3)$$

$$W_0^{\text{twist}}[\chi] = \cos^{-1}[\sin^2(\chi)\cos(W_y) + \cos^2(\chi)] \quad (4.4)$$

where W_y and W_z are the measured FWHM's of the symmetric and in-plane asymmetric rocking curves, respectively. It is further phenomenologically assumed that the tilt of mosaic blocks is exponentially related to their twist about the substrate normal, and conversely. This leads to effective values for $W_0^{\text{tilt}}[\chi]$ and $W_0^{\text{twist}}[\chi]$ given by:

$$W_{\text{eff}}^{\text{tilt}}[\chi] = W_0^{\text{tilt}}[\chi] \exp\left(-m \frac{W_0^{\text{twist}}[\chi]}{\alpha_{\text{twist}}}\right) \quad (4.5)$$

$$W_{\text{eff}}^{\text{twist}}[\chi] = W_0^{\text{twist}}[\chi] \exp\left(-m \frac{W_0^{\text{tilt}}[\chi]}{\alpha_{\text{tilt}}}\right) \quad (4.6)$$

where m is a parameter that describes the dependence of the tilt-twist components, and ranges from -1 (for complete anti-correlation) to 1 (complete correlation). The resulting FWHM of the asymmetric rocking curves is given by

$$W_{\text{resultant}} = \left[\left(W_{\text{eff}}^{\text{tilt}}[\chi] \right)^n + \left(W_{\text{eff}}^{\text{twist}}[\chi] \right)^n \right]^{1/n} \quad (4.7)$$

where $n = 1 + (1 - f)^2$ ranges from 1 to 2 depending on the measured Lorentzian fraction f of the fitted peaks.

The twist angle can be estimated by plotting the FWHM of the asymmetric rocking curves for the reflections $(30\bar{3}2)$, $(10\bar{1}1)$, $(10\bar{1}2)$, $(10\bar{1}3)$, $(10\bar{1}4)$, and $(10\bar{1}5)$, measured in skew-symmetric geometry, versus χ , and using Equations 4.3, 4.4, 4.5 and 4.6 are used to fit Equation 4.7 to the data for α_{twist} and m . This permits estimation of the edge dislocation density N_E via

$$N_E = \frac{\alpha_{\text{twist}}^2}{4.35|\vec{\mathbf{b}}_a|^2} \quad (4.8)$$

where $|\vec{\mathbf{b}}_a| = 3.189\text{\AA}$.

4.2 Atomic force microscopy

To perform local surface characterization of the epilayers, we utilized atomic force microscopy (AFM). AFM is a type of scanning probe microscopy, where a sharp probe tip scans over the sample's surface, producing a magnified image of its topography. AFM images can reveal features including surface defects, dislocations, cracks and steps. The imaging process relies on small-range forces between the outermost atoms of the tip and the sample surface. Typically operating range is 0.1-100 nm, enabling the inference of the tip-sample distance. Depending on the mode of operation, the forces can be attractive (Van der Waals) or repulsive (Pauli repulsion) [58].

The tip is supported from above by a cantilever beam that is adjusted vertically using a feedback correction loop, ensuring a constant force between the tip and the sample during the scanning process. To measure the deflection of the cantilever, the reflected laser light from the cantilever is measured by a photodiode and laser, providing precise information about the distance between the tip and the sample surface and thereby enabling accurate determination of surface feature heights.

AFM can be operated in three modes: a) contact mode, b) non-contact mode, and c) tapping (or intermittent) mode [59]. In the contact mode, the AFM tip makes direct physical contact with the sample's surface, probing the repulsive force regime. This mode is the simplest and offers the advantage of enabling electrical contact with the sample. However, its use carries higher risk of potential damage to either the sample or the AFM tip.

In the non-contact mode an AC voltage is applied to the cantilever at its resonance frequency, inducing small oscillations of the tip with amplitudes of about 0.1 nm, to probe small range attractive forces. These tiny oscillations enable probing small-range attractive forces without contacting the sample surface. Surface feature heights are deduced by measuring the height adjustments of the cantilever beam necessary to maintain a constant oscillation frequency of the AFM [60]. This mode

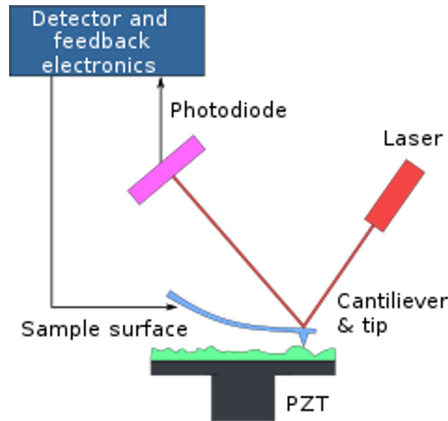


Figure 4.5 The working principle of an AFM.

offers atomic resolution (0.01 nm) in the vertical direction, but requires Ultra-High Vacuum (UHV) conditions and slow scanning to accurately probe such small forces.

In this thesis, the tapping mode is chosen for imaging. It is faster and less demanding than the non-contact mode while providing nanometer-scale transverse resolution, superior to that of the contact mode. In the tapping mode, the cantilever oscillates with an amplitude of about 10-100 nm, allowing it to probe both the contact and non-contact regimes during scans. However, the resonance frequency of the cantilever is influenced by the tip shape, which can change over extended scans due to wear; requiring the use of new tips periodically. It is important to note that AFM images are convolutions of both the tip's and the surface's morphologies, leading to a reduced lateral resolution due to the finite lateral size of the tip [61]. A Bruker AFM with transverse and lateral resolutions of 0.5 nm and 5 nm, respectively, is employed in this work.

4.3 Secondary ion mass spectroscopy

Secondary ion mass spectrometry (SIMS) is used for the determination of concentration profiles of C, Si, O, and H versus depth in the layers. SIMS operates on the principle of physically removing secondary ions from the sample through sputtering with a focused primary ion beam. These secondary ions are then identified through mass spectroscopy and their collection and quantification are measured in counts per second [62]. For depth analysis of element concentrations, a known sputtering rate is applied, and the collection counts-per-time for each element are continuously recorded, providing concentration data as a function of depth in the layers. This process is repeated for all the species of interest. The depth resolutions achieved in SIMS are in the range of 2-10 nm, while lateral resolutions are limited by the beam

size and typically range from 10 nm to 1 μm .

The SIMS measurements in this study were conducted by the Evans Analytical Group laboratories, utilizing a Cs^+ ion beam source with a depth resolution of 10 nm. Typical detection limits for H, C, O, Si were as follows: H: $3 - 5 \cdot 10^{16} \text{cm}^{-3}$, C and O: $1 - 2 \cdot 10^{15} \text{cm}^{-3}$, and Si: $2 \cdot 10^{15} \text{cm}^{-3}$.

4.4 Scanning electron microscopy (SEM)

For fast characterization of surface morphology across larger areas (above 20x20 micrometers), scanning electron microscopy (SEM) is more convenient than (AFM). SEM involves scanning a focused beam of high-energy electrons (5-30 keV) across the surface of the sample. The interactions between the electron beam and the sample generate multiple signals that provide information about the surface's topography and composition [63]. Dedicated detectors collect these signals individually, enabling the construction of SEM images.

'Excitation volume', refers to the three-dimensional region where the interactions between the electron beam and the sample occur. This volume is depicted in Figure 4.6, illustrating the areas from which various signals, such as backscattered electrons (BSEs), secondary electrons (SEs), characteristic X-rays, and Auger electrons, are emitted. The lateral spatial resolution of each SEM signal depends on the size of the excitation volume. This resolution varies progressively from BSEs to SEs to X-rays, as demonstrated by the pear-shaped figure in the illustration.

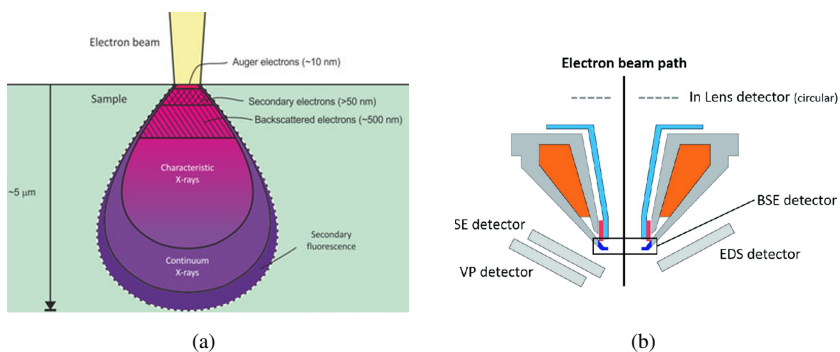


Figure 4.6 Schematic of the excitation volume (a) [64], and the arrangement of the various detectors in a SEM (b) [65].

The size of the excitation volume is influenced by several factors. First, it increases with the beam size at the sample surface (probe size) and the energy of the incoming beam electrons (controlled by the accelerating voltage). On the other hand, the excitation volume decreases with the atomic number of the sample material. For

high-resolution SEM images for a given sample, an optimal balance needs to be achieved where the accelerating voltage is set high enough to generate sufficient signal, while simultaneously being low enough to avoid sample damage and compromising resolution.

BSEs are beam electrons that are elastically (back)-scattered from the atoms in the sample. Their number counts are independent on accelerating voltage, but are highly-sensitive to the atomic number of the sample material. Denser materials with higher atomic number produce more BSEs. High accelerating voltages are employed to collect information from a depth ranging from 0.5-1 micrometers within the sample. As a result, BSEs provide strong compositional contrast, but at relatively low resolution. For detection, BSEs are collected by annular semiconductor detectors positioned vertically above the sample. Employing multiple annular detectors allows the signals to be combined, enabling not only compositional contrast but also the generation of topographical contrast.

The SEs are ejected from the sample due to inelastic interactions of the sample with the impinging electrons. Their energy typically ranges from 0 to 50eV, peaking around 5keV. This energy distribution makes SE images particularly sensitive to the surface morphology, with only SEs originating from depths of approximately 5-50 nm having enough energy to emerge from the sample and be detected. Auger electrons are even less energetic; they emerge from a surface depth of 1 nm. There are two main types of SEs based on their trajectory and escape depth:

- (i) SE1 electrons: These electrons are generated near the point where the electron beam strikes the sample and travel in a generally vertical trajectory from the sample.
- (ii) SE2 electrons: In contrast, SE2 electrons result from the inelastic interactions of backscattered electrons (BSEs) with the sample, arising slightly off the point of incidence.

Due to their distinct generation mechanisms, SE1 images offer better resolution and higher surface sensitivity, as they predominantly represent surface features. On the other hand, SE2 images provide more compositional and topographic contrast at lower resolution, as they are generated from BSEs from deeper regions within the sample.

Both types of SEs are detected using scintillators and photomultipliers. Positive bias is applied to attract the low-energy SE electrons. The SE1 detector is positioned 'in-lens,' located above the sample, while the SE2 detector is positioned off-axis ('side-mounted'). The relative positioning of the detectors results in characteristic differences in images: while all SE images display edge and tilt contrast, SE1 images display a flatter look, emphasizing surface details. In contrast, SE2 images exhibit strong topographical features, 3D look, and compositional contrast.

4.5 X-ray energy dispersive spectroscopy (EDS)

X-ray energy dispersive spectroscopy (EDS) is a quick, easy and versatile bulk composition analysis technique. It relies on the inelastic scattering of incoming beam electrons with the atoms in the sample, and the subsequent emission of characteristic X-rays from relaxation events [66]. When core electrons are ejected following inelastic scattering, the atoms can relax through transitions of electrons from outer-shells to the vacant inner shell, leading to the emission of X-ray photons with energy equal to the energetic difference between the two shells involved in the transition. Given that each atom has known and unique electronic configuration and energy levels, these emissions are characteristic to the elements present in the sample. For EDS performed in a SEM setup, analysing the energies of the emitted X-ray photons allows for the identification of chemical composition. By scanning the SEM probe across an area of the sample, compositional maps can be obtained.

The characteristic emissions show up as peaks in EDS spectra. For each element, multiple electronic transitions are generally possible, resulting in a family of peaks visible in the EDS spectra.

To identify the elements present in the sample, an automatic peak identification procedure is employed. This procedure involves linking each set of family peaks to its corresponding element by referencing tabulated values for the energy levels associated with that element. Before conducting the analysis, the program is provided with information about which elements are expected to be present in the sample. The program filters out any artefact peaks, which may be due to instrument effects or other non-sample-related factors.

A SEM Gemini 500 system equipped with a SiLi p-i-n detector, capable of X-ray photon detection at an energy resolution of 120eV was used for EDS measurements. To maximise X-rays collection efficiency, the detector is positioned in the line-of-sight from the sample (Figure 4.6 (b)). Photon energies were determined by counting the electron-hole pairs generated across the Si bandgap after the absorption of a single X-ray photon, multiplied by the bandgap. Serial photon counting minimized artifact sum peaks in EDS spectra. Before each measurement, the detector was cooled to cryogenic temperatures (-190°C) using liquid nitrogen to minimize thermal carrier generation.

To find the optimal accelerating voltage for EDS measurements on a particular sample, we employed the Casino v3.3 software. This program models the excitation volume for X-rays, based on Monte Carlo simulations of electron trajectories, providing information about the accelerating voltage and sample's structure, including layer arrangement, thickness, and composition.

5

Results and Discussion

5.1 Growth optimization

Initial experiment was conducted in order to study the variation of impurity concentrations and growth rate as a function of the growth conditions in our MOVPE reactor. The goal was the optimization of the growth conditions to minimize background impurity concentrations in the drift layers while maintaining a sufficiently fast homoepitaxial growth rate, and calibrate the actual Si-concentration to the SiH_4 flow rate. For this purpose, a set of GaN layers were consecutively grown on the same GaN substrate, where a single growth condition was varied thrice in each layer, as shown in Figure 5.1 while all other conditions were kept the same. The general growth conditions common for each layer (apart from the parameter being varied) were $T_g = 1040^\circ\text{C}$, $P_g = 225\text{ mbar}$, NH_3 flow = 0.430 mol/min , TMGa flow = $277\text{ }\mu\text{mol/min}$, H_2 flow = 0.640 mol/min .

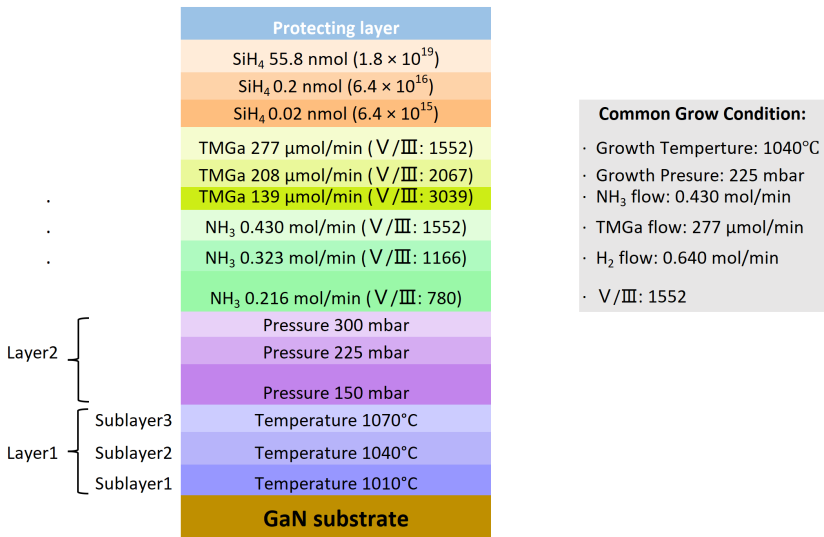


Figure 5.1 Common growth conditions, and a schematic representation of the epitaxial structure grown for SIMS analysis.

The first four layers (above the substrate) were undoped. In Layer 1, the growth temperature was varied in three steps: 1000°C, 1040°C, and 1070°C. In Layer 2, the pressure was varied: 150 mbar, 225 mbar, and 300 mbar. In Layer 3, the ammonia gas molar flow was varied 0.216-0.430 mol/min, while in Layer 4, the TMGa molar flow was varied between 139-277 $\mu\text{mol/min}$. Layer 5 was grown using the common growth conditions listed above, but the silane flow was varied in three steps from 0.02 nmol/min to 55.8 nmol/min. Each of the 15 sub-layers was grown for the same duration of time (335 s). A protecting layer of undoped GaN was grown for 335 seconds on top of the structure, resulting in a total layer thickness of 2.5 μm . The V/III ratio was effectively varied from 780 to 1552 in Layer 3 and from 3093 to 1552 in Layer 4, as a result of the variation in NH_3 and TMGa molar flows, respectively.

The sample was analyzed by SIMS, and the respective depth profiles of C, Si, H, and O concentrations are presented in Figure 5.2. The thicknesses of each sublayer as determined from the SIMS results are indicated in the figure. The average concentration of the impurities were estimated within each sublayer. Using these data, the C and Si impurity concentrations were estimated as a function of the growth parameters. The growth rate for each sublayer was determined by dividing the given sublayer thickness by its growth time (335 seconds).

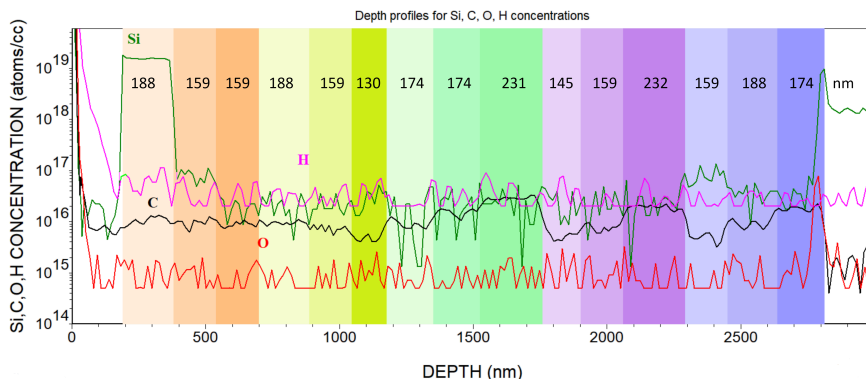
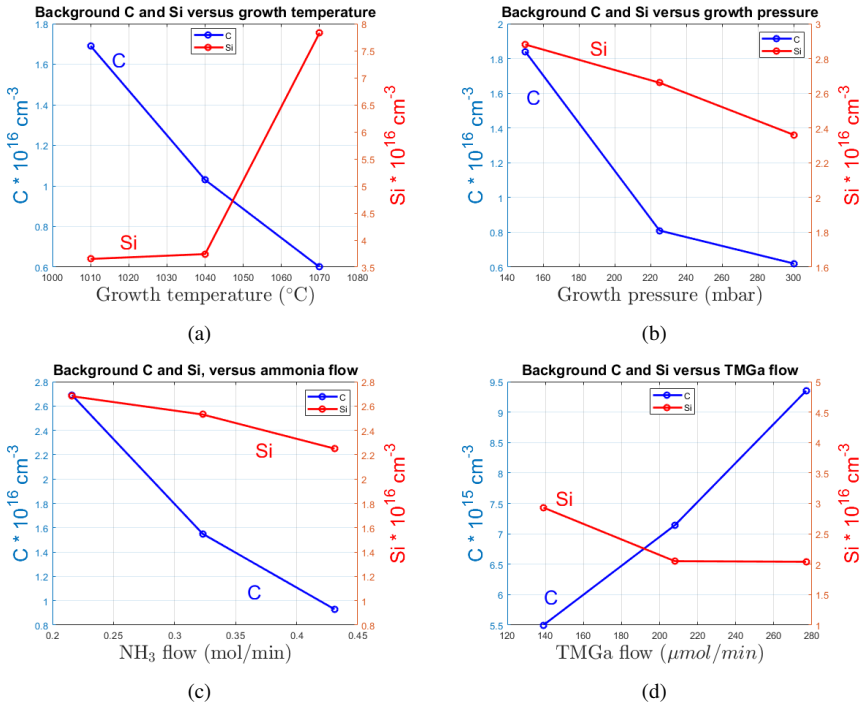


Figure 5.2 The SIMS concentrations for Si (green), C (black), H (pink), and O (red) as a function of depth in the sample. The thicknesses of the sublayers as determined by SIMS are presented in units of nm.

The variation of the background Carbon impurity concentration and (unintentional doping) Si concentration as a function of the growth temperature, pressure, NH_3 molar flow, and TMGa molar flow are shown in Figure 5.1. Figure 5.4 presents the observed variation in growth rate as a function of growth temperature, growth pressure, NH_3 flow and TMGa flows. The variation of the intentional Si concentration as a function of the SiH_4 flow is plotted in Figure 5.5.

Figure 5.1 (d) indicates that the Carbon concentration in Layer 3 increases almost



Note that the scales in the left and right axes can differ by an order of magnitude.

Note that the scales in the left and right axes can differ by an order of magnitude.

Figure 5.3 Background C and Si concentrations versus temperature (a), pressure (b), ammonia flow (c) and TMGa flow (d).

Note that the scales in the left and right axes can differ by an order of magnitude.

linearly in two steps by an overall factor of 1.7 as the TMGa flow is doubled (or as the V/III ratio decreases by a factor of 2), at fixed growth temperature and pressure. This is as expected, since the most important source of C impurities in epilayers grown by MOVPE are the CH₃ molecules (ligands of TMGa) that are produced as TMGa dissociates. More TMGa available, means more incorporation of impurity C atoms. The growth rate also increases almost linearly (Figure 5.4 d) with TMGa flow, suggesting that it is limited by the mass transport of group-III precursors to the surface.

The concentration of residual C decreases by a factor of about 2.8 as the temperature is increased from 1010-1070°C (Figure 5.1 a). A similar decrease is observed as the pressure is raised between 150-300 mbar (Figure 5.1 b), and the ammonia flow from 0.216-0.430 mol/min (Figure 5.1 c). Elevated growth temperatures facilitate gas-phase reactions between ammonia and MO precursors, the by-products of which may be swept out of the chamber before they can diffuse to the surface,

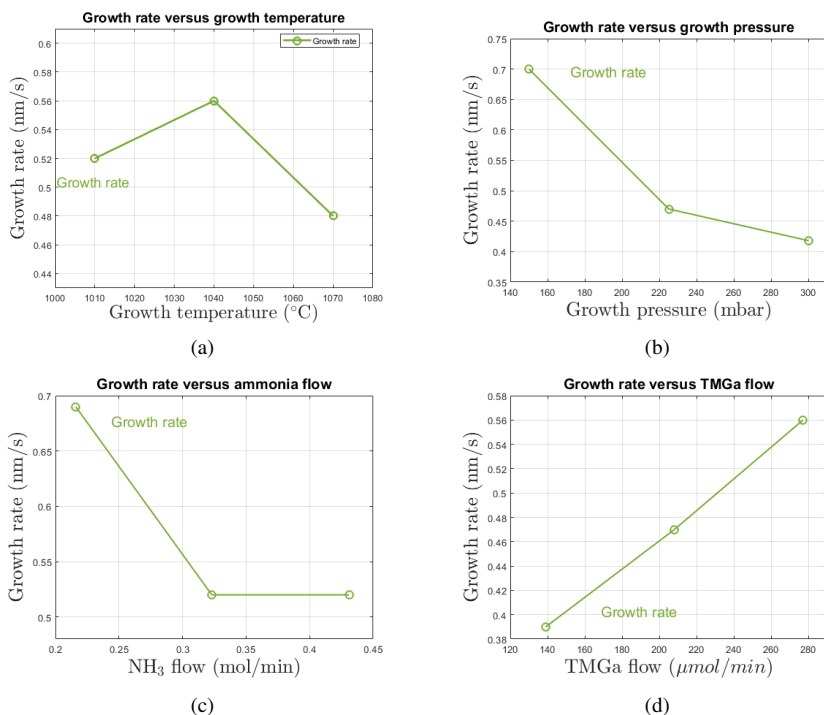


Figure 5.4 Growth rate and background C concentration versus temperature, (a). Growth rate versus pressure (b), ammonia flow (c) and TMGa flow (d). Note that the scales in the left and right axes can differ by an order of magnitude.

leading to a decrease in residual C in the layer. The growth rate is observed to decrease by 15% as the temperature is increased from 1040°C to 1070°C, due to the higher desorption rate of adatoms in the evaporation regime. High temperatures also enhance the thermal decomposition of H_2 and NH_3 . Methyl groups formed by combinations of atomic hydrogen with Carbon atoms can desorb from the surface in the evaporation regime, further reducing the Carbon concentration [67]. More atomic hydrogen is available from dissociation at higher ammonia flows – this may explain the observed decrease in C concentration with NH_3 flow (Figure 5.1 c) and of the growth rate (Figure 5.4 c). Higher growth pressures lead to a thicker boundary layer and a more turbulent flow, which promote parasitic gas-phase reactions and enhanced deposition on the reactor sidewalls, thereby decreasing both the growth rate (Figure 5.4 b) and the Carbon concentration (Figure 5.1 b).

No significant variations are observed for the concentrations of H and O as a function of the growth conditions. Their respective values were found to be $3.4 \times 10^{16} \text{cm}^{-3}$ and $9.6 \times 10^{14} \text{cm}^{-3}$ on average throughout the structure. These are near the respective detection limits of SIMS.

The concentration of unintentional background Si is observed to increase with growth temperature (Figure 5.1 a). This may be associated with an increase in the number of Ga vacancies available for Si atoms to occupy. On the other hand, a decrease in background Si concentration occurs with increasing TMGa flow rates (Figure 5.1 d). A similar trend is also observed at higher NH₃ flow rates (Figure 5.1 c). It was reported that such an effect could be attributed to N atoms occupying Ga vacancies instead of Si [68].

These observed trends should be generally applicable to other MOVPE reactors, but the actual numerical values may vary between reactors. Our results highlight the expected anti-correlation between the growth rate and background Carbon concentration. When developing thick drift layers for vertical power devices, a faster growth rate is advantageous, but it should not come at the cost of increasing the point defect density. The results show that the common growth conditions strike a satisfactory equilibrium between these two competing factors.

In this initial growth run, each (sub)layer was grown at different growth conditions with respect to the (sub)layer below. As a result, the surface roughness and dislocation densities – both of which may affect the incorporation of impurities in the grown epilayers – may vary between (sub)layers. A more precise investigation of impurity incorporation as a function of the growth conditions, that would improve result comparisons, would involve SIMS analysis of separate individual layers on identical GaN substrates. The latter approach is impractical however, due to the high cost of GaN substrates and SIMS measurements. The average thickness of the sublayers (about 200 nm) is close to the depth resolution of SIMS. This poses challenges in precisely identifying the spatial boundaries of sublayers, making it harder to reliably determine the concentrations of impurity atoms within them. Opting for thicker sublayers is also not a practical solution as it would substantially increase the expensive MOVPE growth time.

For better optimization of the growth conditions to reduce impurity concentrations, in addition to more data points, the incorporation of impurities as a function of the H₂ flow could also be investigated. In this thesis work, a 100% H₂ carrier gas flow was chosen to achieve a higher growth rate due to its lower viscosity compared to N₂. A H₂ flow of 0.640 mol/min was maintained for each growth run. However, both Carbon incorporation and growth rate are influenced by the H₂ flow [69]. H₂ flow determines the degree of reactant dilution and the available reaction time at the wafer surface [70], thereby directly affecting the incorporation of impurities during the growth process.

For the growth runs in this thesis, the stated common growth conditions are evidently optimal on the basis of the results in Figure 5.5. They serve to maintain a balance between minimizing the residual Si and C incorporation and maximizing the growth rate. These conditions predict a C concentration of $1.1 \times 10^{16} \text{cm}^{-3}$ and a residual Si concentration of $2.7 \times 10^{16} \text{cm}^{-3}$. Therefore, ignoring the small

contribution from O residual impurities and that of H, the overall expected n-type doping concentration in unintentionally doped GaN under these growth conditions is $N_{\text{d-Na}} = 1.6 \times 10^{16} \text{ cm}^{-3}$, assuming that all Carbon behaves as acceptors and are activated.

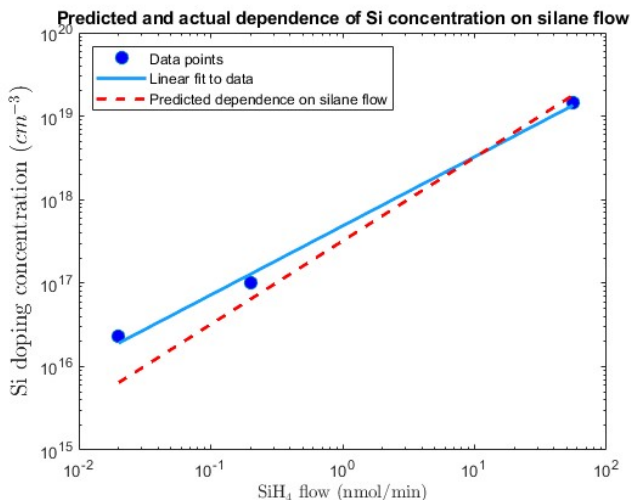


Figure 5.5 Intentional Si concentration versus silane flow (blue dots). A linear fit to the data is shown in blue color, while the red dashed line is the expectation from basic theory.

Figure 5.5 indicates that the logarithm of the (intentional) Si concentration, $[\text{Si}]$, is linearly dependent on the logarithmic molar flow rate of SiH_4 over the range of 0.02 nmol/sec to 55.8 nmol/sec under the optimal growth conditions. A linear fit to the data (blue line) reveals that $\log([\text{Si}]) = 0.83 \times \log(\chi_{\text{SiH}_4}) + 17.6851$. In practice, this allows for a straightforward calibration of the molar flow rate of SiH_4 to the actual Si concentration in the layers. For the thick ($5\mu\text{m}$) drift layers, an overall n-type doping concentration of $4.6 \times 10^{16} \text{ cm}^{-3}$ was desired to improve the resistance in the ON state. Hence a molar flow rate of 0.059 nmol/min for silane was used, and these layers are referred to as n-doped. A silane flow of 27.9 nmol/min was used to obtain a desired doping concentration of $7.5 \times 10^{18} \text{ cm}^{-3}$ in a thin surface layer on the top of the drift layer in order to enable ohmic contacts and improve the contact resistance. Figure 5.5 suggests that Si incorporation exceeds what is expected from theory (dashed red line) at small flows, and is below what is expected from theory at higher flows. More data points are required for a better comparison, at these growth conditions. It is important to note that, while in theory GaN offers up to about 4.5×10^{22} Ga substitutional sites per cm^{-3} of material, compensation due to native defects (e.g., V_{Ga} , V_{N}) limits the possible n-type doping concentrations to below about 10^{20} cm^{-3} [32].

5.2 GaN and AlGaN epitaxy

Figure 5.5 presents an overview of the epitaxial structures of different GaN and AlGaN drift layers studied in the thesis. In all cases the growth is performed on (0001) oriented, flat $1\text{cm} \times 1\text{cm}$ diced, HVPE-grown, $325\ \mu\text{m}$ thick n^+ doped GaN substrates (with a Si doping concentration of $3 \times 10^{18}\text{cm}^{-3}$). All drift layers were Si-doped with intended donor concentration of about $4.6 \times 10^{16}\text{cm}^{-3}$ (n^- doped).

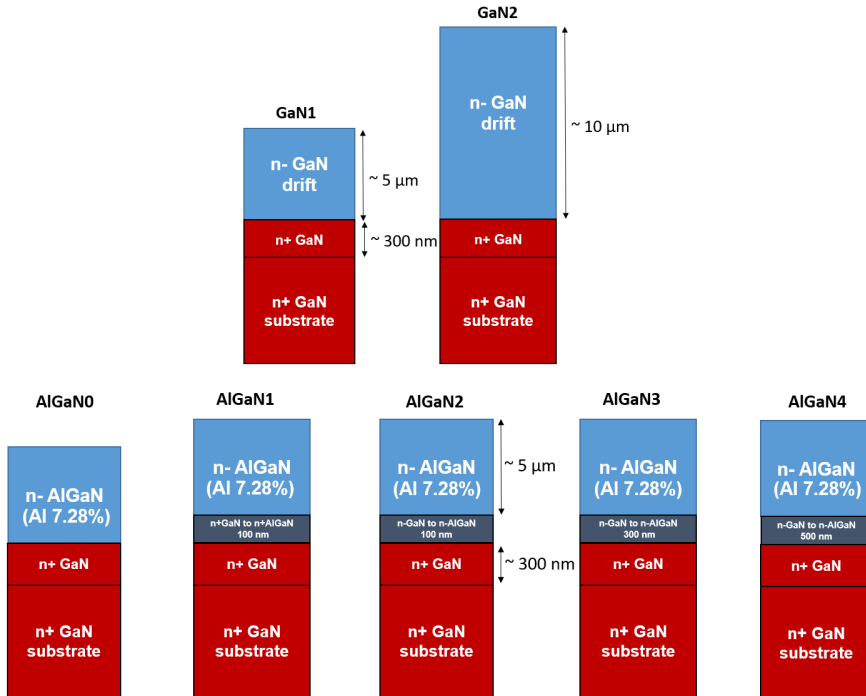


Figure 5.6 Schematic representations of the epitaxial structures studied in the thesis: top row - GaN and bottom row - AlGaN drift layers.

Prior to growth, the substrates underwent a thorough cleaning process involving ultrasonic cleaning with acetone, IPA, and DI water, followed by Piranha etching for 25 minutes at $100\ ^\circ\text{C}$. This cleaning step was needed to remove any organic contamination present and residuals from the dicing process. Furthermore, before the growth process, and during cooldown to room temperature after growth has been completed, all substrates were subjected to a high-temperature ammonia flow treatment. Specifically, an ammonia flow of $0.430\text{mol}/\text{min}$ along with an H_2 carrier gas flow of $0.640\text{mol}/\text{min}$ was applied for 850 seconds as the reactor temperature is ramped up to growth temperature (1040°C). This nitridation treatment is performed mainly to reduce the deficiency in Nitrogen due to evaporation from the surface [71],

Table 5.1 Common growth conditions of the the GaN n⁺ nucleation and the (Al)GaN drift layers for all the samples.

Layer	Growth Temperature (°C)	Growth Pressure (mbar)	NH ₃ Flow (mol/min)	TMGa Flow (μmol/min)	H ₂ Flow (mol/min)	SiH ₄ Flow (nmol/min)	Growth Time (s)	Growth Rate (nm/s)
n ⁺ GaN	1040	225	0.430	277	0.640	27.9	540	0.56
n ⁻ GaNdriftlayer	1040	225	0.430	277	0.640	0.059	9000	0.56
n ⁻ AlGaNdriftlayer	1040	225	0.430	277	0.640	0.059	8200	0.62

and it offers various other benefits, including: i) facilitating surface reconstructions, thereby contributing to the reduction in the number of surface defects and improving surface roughness; ii) facilitating the annihilation of dislocations, improving crystal quality, and iii) enabling the removal of unintended impurities at the GaN substrate surface.

In all samples, a common feature is the growth of a 300 nm n⁺ GaN layer on top of the substrate, referred to as the *nucleation layer*, which is doped with Si to a concentration of $7.6 \times 10^{18} \text{cm}^{-3}$. This doping level is chosen to improve drain contact resistance while ensuring it does not negatively impact the quality of the epitaxial layers on top. Previous studies [72] have demonstrated that doping concentrations in the range of $1 - 3 \times 10^{19} \text{cm}^{-3}$ using Si can have a degrading effect on both the crystal quality and surface morphology, and these effects extend to the epitaxial layers; the doping concentration in the nucleation layer was therefore limited below such value. The growth conditions for the different drift layers were also common to all the samples. Table 5.1 summarizes the common growth conditions for both the nucleation and the main drift layers. Both, the GaN and the AlGaN samples were cooled from 1040°C down to 400°C at the same rate of 64°C/min. A further 20 minutes were needed to cool the reactor down to room temperature.

As mentioned above, the growth conditions for the drift layer serve to maintain a balance between minimising the residual Si and C incorporation and maximising the growth rate. GaN growth necessitates temperatures exceeding 1000°C due to several factors. First, high temperatures supply sufficient thermal energy to promote rapid GaN-forming reactions, ensuring growth occurs within the mass transport regime. Moreover, the thermal decomposition of ammonia, a key component in the process, requires such elevated temperatures to proceed at an optimal rate [73]. Additionally, the higher temperatures enhance the mobility of adatoms, enabling 2D growth of high-quality planar GaN epilayers with improved surface morphology and crystalline quality [74]. Furthermore, elevated temperatures aid in reducing background Carbon incorporation during the growth process [13]. However, even higher temperatures can lead to a rougher surface morphology due to the evaporation of species from the substrate, as evidenced by previous results in our group when utilizing growth temperatures of 1100°C.

The first sample series consists of two 5 μm- and 10 μm-thick GaN drift layers - samples GaN1 and GaN2 (see Figure 5.5 top row). The only difference between the two layers is that the n⁻ drift layer of GaN2 was grown for nearly twice the time

(17500 s) as compared to GaN1, resulting in an expected layer thickness of about $10\ \mu\text{m}$. Since both layers were grown at the same optimised growth conditions, they should have very similar doping properties (charge carrier concentration and mobility) and hence a twofold increase in breakdown voltage for GaN2 with respect to GaN1 could be expected. It should be noted that larger thickness of the drift layer would also result in an increase of on-resistance due to the longer current path in GaN2. Hence, further adjustment of doping may be needed for an optimized device performance based on $10\ \mu\text{m}$ -thick drift layers, which however, is beyond the scope of this thesis. Representative optical microscopy images ($4\times 4\ \text{mm}$) taken at the centre of the samples are shown in Figure 5.7 revealing that the homoepitaxial layers GaN1 and GaN2 are found to be crack-free as expected.

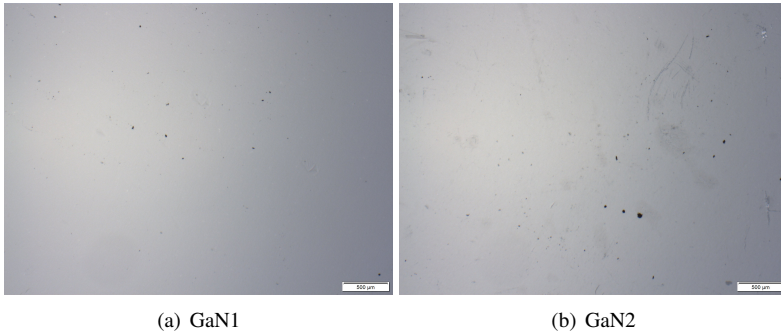


Figure 5.7 Representative $4\ \text{mm}\times 4\ \text{mm}$ optical microscopy images of the samples from the GaN-on-GaN series. Scale bar is $500\ \mu\text{m}$ in length.

In a second series, $5\ \mu\text{m}$ AlGaN drift layers were grown, samples AlGaN0 to AlGaN4 (see Figure 5.5 bottom row) with an intended Al content of about 8%. For this purpose, a TMAI flow of 100 ccm was introduced during the growth of the drift layers while all other growth conditions were kept the same (see Table 5.1). The drift layers in this case were grown for 8200 s to compensate for the faster growth rate as compared to GaN (1.126 times faster) resulting from the additional TMAI. While the added TMAI introduces higher growth rates, the Al adatom mobility is expected to be lower compared to Ga under these growth conditions [75]. As a result, the growth time of 8200 s was chosen, instead of 7992 s, to achieve the desired $5\ \mu\text{m}$ layer thickness.

The primary objective of alloying with small amount of Al in the second series of samples was to increase the critical electric field in the drift layers without significantly affecting the free charge carrier concentration and mobility with respect to GaN, thus enhancing their Baliga's figure of merit (BFOM) relative to the $5\ \mu\text{m}$ drift layers (GaN1). Recently, it has been demonstrated that in low-Al-content (6% – 8%) AlGaN-on-SiC, electron mobility is primarily limited by the dislocation density rather than alloy scattering resulting in similar or even higher BFOM than

GaN [76]. By employing GaN substrates for the AlGaIn drift layers growth here we aim at reducing the dislocation densities with respect to the heteroepitaxy on SiC and hence further improving mobility parameters and BFOM.

In the sample denoted as AlGaIn0 (Figure 5.5 - bottom row) the drift layer was grown directly on the GaN n^+ nucleation layer without any buffer layer. This sample was found to display a surface crack. In an attempt to grow crack-free $5\mu\text{m}$ -thick layers beyond the critical thickness for plastic deformation, the rest of the AlGaIn samples were grown with a compositionally graded buffer layers with Al content between 0 and 8% prior to the main drift layer growth. The grading process was performed continuously i.e. the molar flow of TMAI was increased continuously from zero to $35.6\mu\text{mol}/\text{min}$. In AlGaIn1 and AlGaIn2 the doping of the compositionally graded buffer layer with a thickness of 100 nm, i.e. growth time of 180s, was varied with n^+ , i.e. $[\text{Si}] = 7.6 \times 10^{18} \text{cm}^{-3}$ for AlGaIn1 and n^- , i.e. $[\text{Si}] = 4.6 \times 10^{16} \text{cm}^{-3}$ for AlGaIn2. It was observed that AlGaIn1 exhibited a surface crack, while AlGaIn2 did not display any cracks. However, during handling of the sample at a later stage, it broke, which led us to conclude that likely internal crack may have been present. Indeed, after breaking additional crack appear in the AlGaIn2 sample. Consequently, further optimization of the compositionally graded n^- buffer layer was focused on varying its thickness. The subsequently grown samples AlGaIn3 and AlGaIn4 included thicker n^- doped compositionally graded buffer layer of thicknesses of 300 nm (growth time of 540s) and 500 nm (growth time of 900s), respectively.

Representative optical microscopy images ($4\text{ mm} \times 4\text{ mm}$) taken at the centre of the AlGaIn series samples are shown in Figure 5.8, and summarised graphically in Figure 5.9. Figure 5.8 (a) represents well the surface of both AlGaIn0 and AlGaIn1. As can be seen the images illustrate a network of cracks spread through the centre of the drift layers of all AlGaIn samples apart from AlGaIn3. We note that although the whole central region of the AlGaIn3 sample is crack-free, at its edges occasional small cracks can be found. Such edge effects were previously observed for different epitaxial structures in multiple reactors and could be associated with slight thickness non-uniformities. Typically, this issue is mitigated by use of larger wafers. The n^- doped, continuous graded layer of about 300 nm seems to effectively minimize the crack density in the AlGaIn-on-GaN drift layers, compared to its counterparts of 100 nm and 500 nm, and the n^+ 100 nm-thick buffer layer, grown under the same conditions and cooled at the same rate. Apparently, the 100 nm-thick graded layer is too thin to accommodate the tensile strain accumulated during the cooling down to room temperature, and that increasing the buffer layer thickness above 300 nm to 500 nm is not beneficial. Concerning the n^+ graded buffer layer, it should be noted that high Si concentrations in GaN epilayers have been found to expand the GaN lattice i.e. to cause tensile strain [77]. This effect could potentially be responsible for the observed cracks in AlGaIn1. The cracks could be attributed to the heightened tensile strain in AlGaIn layers resulting from the increased lattice mismatch with GaN. This mismatch could be too large for a 100 nm-thick buffer layer to adequately

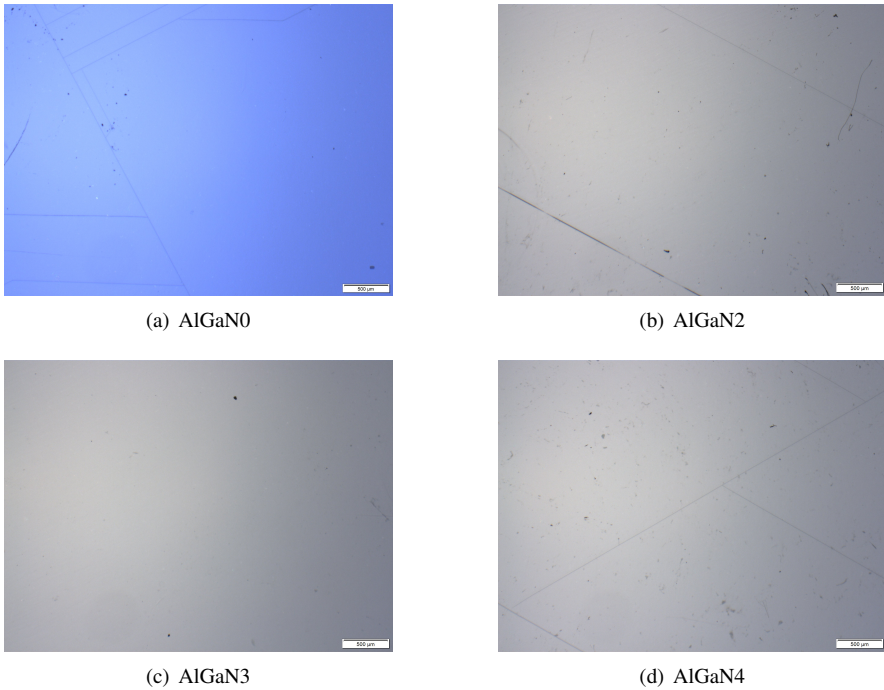


Figure 5.8 Representative 4 mm×4 mm optical microscopy images of the samples from the AlGaN-on-GaN series. Scale bar is 500 μm in length.

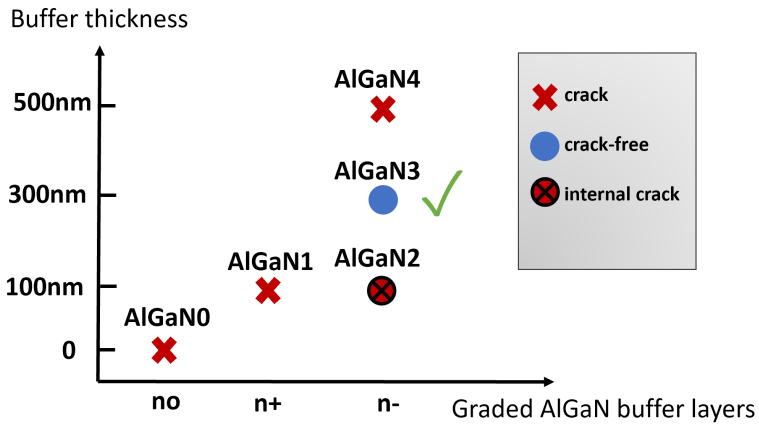


Figure 5.9 Crack status in the AlGaN series versus the doping type of graded AlGaN buffer layers.

manage.

5.3 Structural properties of the drift layers

The following samples GaN1, GaN2, AlGaN2, AlGaN3, and AlGaN4, as well as the GaN substrate, were selected for additional characterization by SEM, EDS, and XRD.

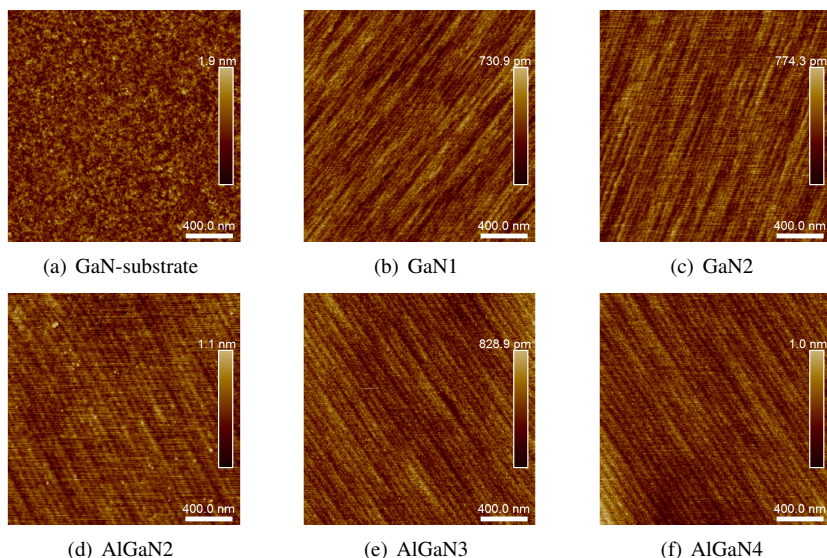


Figure 5.10 Representative $2\mu\text{m}\times 2\mu\text{m}$ tapping-mode AFM images taken in a central region of the samples. Note that the color bars symbolise different vertical scales in each of the scans.

The surface morphology of the drift layers and the GaN-substrate was evaluated using tapping-mode AFM in air, and shown in Figure 5.10. The $2\mu\text{m}\times 2\mu\text{m}$ images, taken within a region near the centre of the samples, indicate epilayers with smooth surfaces superior to the substrate. Long, uniform and well-defined atomic steps are observed for the epilayers, and no pits (dislocations). Surface roughness (the mean height difference in peaks and valleys over the surface) is quantified by a root-mean-square value (Rq). GaN1, GaN2, and AlGaN3 exhibit Rq values of 0.105 nm and 0.112 nm respectively, which are smaller by more than a factor of two than that of the GaN-substrate (0.274nm). The surface roughness of the epilayers in AlGaN2 (0.154nm) and AlGaN4 (0.134) is higher by about 20%; which may be related to their higher surface crack density.

A $20\mu\text{m}\times 20\mu\text{m}$ SEM (SE2) image taken at the centre of AlGaIn3 (Figure 5.11 (a)) exhibits a surface free of any dislocations, which are typically visible as pits (black spots) in SE2 images. SE2 images taken in other areas of the sample give no new information, except near the edges, where some dislocations are present. The other 5 samples show similar morphology in SEM. For Al content estimation of AlGaIn3, an EDS map-scan was performed over a crack-free 1 mm^2 central area of AlGaIn3. Figure 5.11 (b) and (c) show uniform Al content over the sample. A uniform AlN composition of 7.28 % was estimated from the EDS spectra. This value is in good agreement with the intended composition of 8% being slightly lower. The AlGaIn drift layer was grown at the same growth conditions as GaN, while Al is known to require comparatively lower pressures to reduce the losses due to gas-phase reactions [78] or/and higher growth temperatures to enhance Al adatom mobility on the surface and facilitate its incorporation in the crystal lattice.

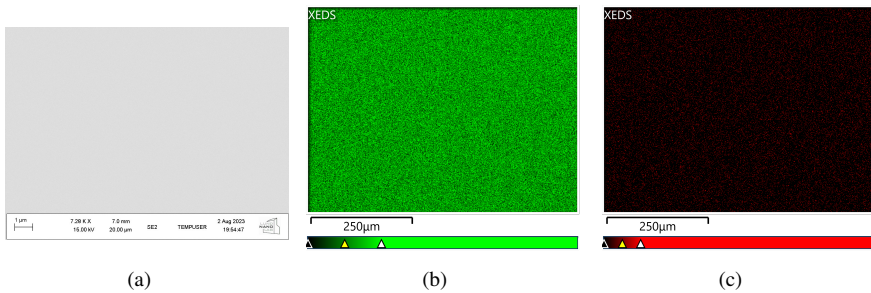


Figure 5.11 SEM image of AlGaIn3 taken in a central region of the sample (a) and corresponding EDS compositional maps of Ga (b) and Al (c).

The XRD results are presented in Table 5.2, Figure 5.12 and 5.13 (a-c) shows the corresponding plots and comparisons. Figure 5.13 (d) indicates a decrease in the FWHMs of the symmetric rocking curves with increasing diffraction order for GaN-substrate. Surprisingly, the FWHMs of the asymmetric rocking curves also decreased with the diffraction order, a trend observed in all five samples. This observation contradicts the initial expectation, as the mosaic model predicts broadening of diffraction peaks with higher order reflections. Considering that the penetration depth of the X-rays increases with the Bragg angle, one possible explanation for this unexpected behavior is that the surface region of the samples may have lower screw and edge dislocation densities compared to the bulk. However, it is also likely that the mosaicity model does not accurately describe our low-dislocation-density samples.

Nonetheless, it is instructive to estimate the screw and edge (mixed) dislocation densities of the epilayers and GaN substrate using the method described in [79], with the twist and tilt angles substituted by the FWHM – measured in radians – of the (002) and (101) rocking curves, in equations 4.5 and 4.8, respectively. It is essential

Table 5.2 2θ peak positions and FWHMs of the RCs and $2\theta - \omega$ scans for the drift layer samples and the GaN-substrate. The FWHM values may overestimate the dislocation densities in the epilayers*.

	FWHM (arcsec)			2θ Peak Positions ($^{\circ}$)		
	(002) RC	(101) RC	(002) $2\theta - \omega$	(101) $2\theta - \omega$	(002) $2\theta - \omega$	(101) $2\theta - \omega$
GaN-substrate	44.93	60.91	43.16	32.00	34.57725	36.85019
GaN1	90.54	35.35	43.74	37.87	34.57476	36.85067
GaN2	66.38	83.20	40.36	31.97	34.57463	36.84718
AlGaN2	34.56	-	52.06	66.13	34.65771	36.87229
AlGaN3	40.25	-	54.58	45.11	34.65918	36.87303
AlGaN4	36.65	-	46.48	34.48	34.65784	36.87138

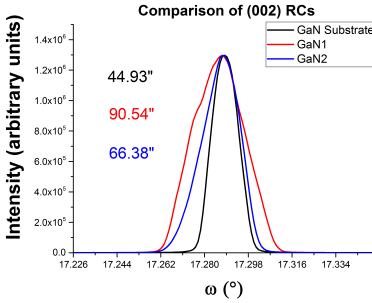
* The FWHM for the (101) RC of AlGaN samples could not be taken due to the instrument being down.

to note that these estimates are likely overestimates of the dislocation densities in the epilayers, as explained below. The results are listed in Table 5.2 and 5.3. We recall the reader that the full width half maxima of (0002) and (10 $\bar{1}$ 1) - referred to from hereon-in as (002) and (101) for simplicity - RCs allow for the estimation of screw and edge (mixed) dislocation densities, respectively. The broadening of the (002) and (101) $2\theta - \omega$ peaks on the other hand, relates to the vertical and lateral (mixed) coherence lengths of the mosaic blocks, respectively.

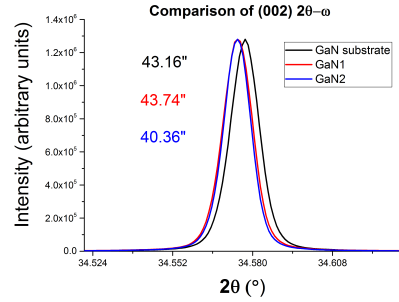
Table 5.3 Screw and edge (+mixed) dislocation densities for the samples.

	Screw dislocation density / cm^{-2}	Edge dislocation density / cm^{-2}
GaN-substrate	4.1×10^6	2.0×10^7
GaN1	1.6×10^7	6.6×10^6
GaN2	8.9×10^6	3.7×10^7
AlGaN2	2.4×10^6	-
AlGaN3	3.3×10^6	-
AlGaN4	2.7×10^6	-

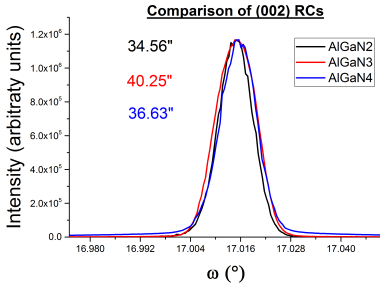
In Figure 5.12 (a), the (002) rocking curves of the GaN-substrate, GaN1, and GaN2, are compared. The (002) RC FWHM for GaN1 (90.54 arcsec) is nearly double that of the GaN substrate (44.93 arcsec) but only 30% higher than that of GaN2 (66.38 arcsec). Considering a penetration depth of $10\mu\text{m}$ for (002) reflections (as discussed in Section 4.1.2, the substrate is expected to contribute to the broadening of the rocking curves, in addition to the broadening due to the epilayers. This contribution is expected to be greater for GaN1 ($5\mu\text{m}$ thick epilayer) compared to GaN2 ($10\mu\text{m}$ thick epilayer), but no greater than 34.56 arcsec (the (002) FWHM of the AlGaN2 RC). Therefore, it seems likely that the GaN epilayers, grown under our conditions, have similar (if not better, as observed in [9]) screw dislocation densities as the GaN substrate.



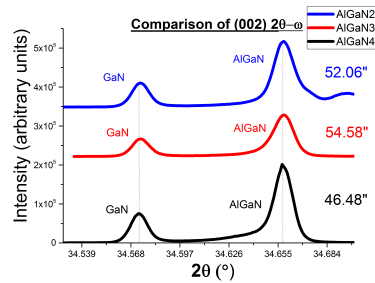
(a) GaN-substrate, GaN1-2 (002) rocking curves



(b) GaN-substrate, GaN1-2 (002) 2θ - ω curves



(c) AlGa2-4 (002) rocking curves



(d) AlGa2-4 (002) 2θ - ω curves

Figure 5.12 RC and 2θ - ω curves for GaN-substrate, GaN1-2, and AlGa2-4.

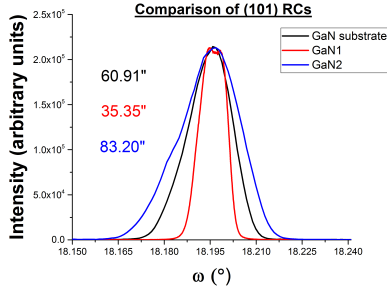
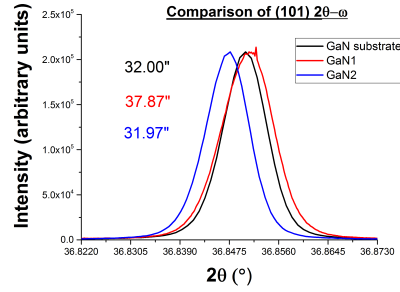
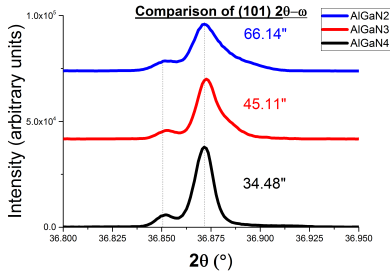
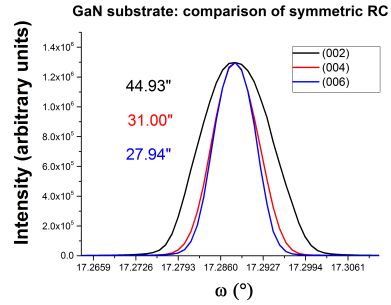
Reflections from (101) planes in GaN are observed at a Bragg angle of 18.4348 degrees and a χ angle of 61.99 degrees, resulting in a penetration depth of approximately 5 μm . Therefore, the observed FWHMs for the (101) rocking curves (RC) of GaN1 (35.35 arcsec) and GaN2 (83.20 arcsec) can probably be attributed solely to dislocations in the epilayers. The (101) RC FWHM of the substrate (60.91 arcsec) is nearly twice that of GaN1, suggesting a significant improvement by a factor of 3 in the edge (mixed) dislocation density of the epilayer. However, the GaN2 epilayer shows nearly double the edge (mixed) dislocation density compared to the substrate. It is probable that the side facet of the sample facing the beam was damaged, causing an additional tilt in the crystallites. A repetition of this measurement with a different ϕ angle is necessary to confirm the high value for the FWHM of the (101) RC of GaN2. Unfortunately, this confirmation was not possible since the instrument was broken. The (101) RCs of the AlGaN1, AlGaN2, and AlGaN3 samples could not be taken for the same reason.

Figure 5.12 (c) compares the (002) RC FWHMs for AlGaN2 (34.56 arcsec), AlGaN3 (40.25 arcsec), and AlGaN4 (36.65 arcsec), which correspond to screw dislocation densities of $2.4 \times 10^6 \text{cm}^{-2}$, $3.3 \times 10^6 \text{cm}^{-2}$, and $2.7 \times 10^6 \text{cm}^{-2}$, respectively, for

the AlGa_N epilayers (including the contribution from the substrate). These values are lower than the screw dislocation density of the GaN substrate ($4.1 \times 10^6 \text{ cm}^{-2}$), indicating that the $5 \mu\text{m}$ AlGa_N epilayers have better screw dislocation densities than the respective substrates. Among the three AlGa_N samples, AlGa_N3 appears to have slightly higher screw dislocation density, approximately 1.5 times higher than those of AlGa_N2 and AlGa_N4. This observation is supported by a comparison of the FWHM values for the (002) $2\theta - \omega$ curves of AlGa_N2 (52.06 arcsec), AlGa_N3 (54.58 arcsec), and AlGa_N4 (46.48 arcsec) (see Figure 5.12 d), suggesting that AlGa_N3 has slightly smaller vertical coherence length as compared to the other AlGa_N samples. The growth of low Al-composition AlGa_N at 1040°C is believed to be pseudomorphic; however, cracking occurs during the cooldown of the reactor to room temperature due to tensile strain. It seems plausible that the release of strain energy through crack formation leads to lower threading dislocation densities in the epilayer, as less strain energy is available for their formation. As a result, the epilayers appear better structurally. However, cracked layers are not suitable for device fabrication and the lower dislocation densities in this case are not an advantage. Another possible explanation for the observed small differences in RC and radial scans broadenings between the different AlGa_N samples could be a variation in dislocation densities of the respective substrates. We recall that the GaN substrates used here are fabricated by HVPE method, which is based on heteroepitaxy and subsequent removal of the substrate to produce the quasi-bulk GaN material. Hence, a certain spread in dislocation density or in general in structural quality over the 4-inch GaN free-standing wafer, from which the $1 \text{ cm} \times 1 \text{ cm}$ substrates used here were cut, is possible. Experiments, involving simultaneous growth on multiple $1 \text{ cm} \times 1 \text{ cm}$ GaN substrates for each of the AlGa_N drift layers could provide a more conclusive answer but are not practical from a cost perspective.

Let us now turn our attention to the (101) $2\theta - \omega$ scans, which are broadened by both limited lateral and vertical coherence lengths. The FWHMs were found to gradually decrease with increasing the thickness of the n^- -graded buffer layer with 66.13 arcsec for AlGa_N2, 45.11 arcsec for AlGa_N3, and 38.48 arcsec AlGa_N4 (see Figure 5.13 (c)). However, it is important to note that the fit for AlGa_N2 was the least reliable among all fits. Additionally, variations in the crystal quality of the substrates on which the five samples are grown could also affect these results as mentioned earlier.

In Figure 5.12 (b), the FWHM values for the (002) $2\theta - \omega$ curves of the GaN-substrate (43.16 arcsec), GaN1 (43.74 arcsec), and GaN2 (40.36 arcsec) are compared, along with their positions (see Table 5.2). The positions of the (002) $\omega - 2\theta$ peaks for these three samples are similar within 10 arcsec. This similarity also applies to the positions of the (101) $2\theta - \omega$ peaks of the same samples (Figure 5.13 b), which is to be expected as no significant additional strain is anticipated in homoepitaxy.


 (a) GaN-substrate, GaN1-2 (10 $\bar{1}$ 2) rocking curves

 (b) GaN-substrate, GaN1-2 (10 $\bar{1}$ 1) $2\theta - \omega$ curves

 (c) AlGaIn2-4 (10 $\bar{1}$ 1) $2\theta - \omega$ curves


(d) GaN-substrate, rocking curves

Figure 5.13 RC and $2\theta - \omega$ curves for GaN-substrate, GaN1-2, and AlGaIn2-4.

Figure 5.13 (b) compares the FWHM values for the (101) $2\theta - \omega$ curves of the GaN-substrate (32.00 arcsec), GaN1 (37.87 arcsec), and GaN2 (31.97 arcsec). With the penetration depth being about 10 μm , the FWHM results for the (002) and (101) $\omega - 2\theta$ suggest an improvement in the coherence lengths. However, this conclusion is uncertain due to small differences in Bragg peak positions of the sample. Minute differences in Bragg peak positions have a large effect on the calculation of coherence lengths.

6

Summary and outlook

High-quality GaN drift layers, 5 μm and 10 μm thick for vertical power devices, were homoepitaxially grown with RMS surface roughnesses on the order of 0.1 nm and screw dislocation densities comparable to or better than the substrate. Additionally, the edge dislocation densities were potentially better than the substrate. The growth conditions were optimized to minimize background impurity incorporation (except for the H_2 flow), resulting in a growth rate of 0.56 nm/s and an expected Nd - Na background doping concentration of $1.6 \times 10^{16} \text{cm}^{-3}$ in u-GaN. The intentional Si concentration was calibrated to the silane molar flow to achieve a relatively low and controlled n-doping of the GaN drift layers to approximately $4.6 \times 10^{16} \text{cm}^{-3}$. While growth rates twice as high as ours at background carbon concentrations below 10^{16}cm^{-3} have been achieved in other studies [80], our surface roughness and edge dislocation density values are highly competitive. For a fuller analysis, further study should investigate the growth rate and background impurity concentrations as a function of H_2 flow, using thicker sublayers and more data points.

Subsequently, using the same growth conditions as for the n-doped GaN drift layers, 5 μm layers with approximately 7.28% AlN composition were heteroepitaxially grown on GaN to enhance the BFOM for power devices. It was found that a continuous (n⁻ doped) grading layer, approximately 300 nm in thickness, worked best to minimize the AlGaIn epilayer surface crack density, although it still exhibited some cracking at the edges. To enable the growth of even thicker AlGaIn-on-GaN drift layers, a deeper understanding of the mechanisms governing crack formation and propagation in AlGaIn, and their correlation with growth conditions, is essential. One potential improvement could involve a slower cooling rate to promote gradual strain relaxation. Another approach may include growing grading layers at lower temperatures to facilitate 3D growth. While this may result in a rougher surface morphology of the grading layer, it could offer better control of strain. Lower temperatures, however, are associated with a higher background carbon concentration, which is not desirable.

One strategy for enhancing conduction involves the growth of higher-doped grading layers to smoothen out the conduction band discontinuity at the AlGaIn-GaN heterojunction, thereby enhancing carrier mobility. However, caution is necessary to prevent excessive doping that could compromise strain engineering efforts. The growth conditions for the AlGaIn-on-GaN samples were identical to those for GaN1

and GaN₂. To optimize the growth conditions for minimizing residual impurities in AlGa_N, a SIMS analysis is also necessary. This will also allow to establish a comprehensive understanding of the Al incorporation on AlGa_N as a function of growth parameters, which is crucial for better control of the Al content in AlGa_N.

Next steps include fabrication and characterization of FIN field effect transistors based on the epitaxial structures of GaN₁, GaN₂ and AlGa_{N3}, which will also provide insights into the drift layer properties and need of further material optimization.

Bibliography

- [1] J. Lutz, H. Schlangenotto, U. Scheuermann, and R. De Doncker. “Semiconductor power devices”. *Physics, characteristics, reliability* **2** (2011).
- [2] N. Mohan. “Introduction to power electronics”. In: *Proceedings of the American Power Conference*. Vol. 59. 1997, pp. 718–721.
- [3] G. Meneghesso, M. Meneghini, and E. Zanoni. “Power gan devices materials, applications and reliability” (2017).
- [4] B. J. Baliga. *Fundamentals of power semiconductor devices*. Springer Science & Business Media, 2010.
- [5] M. Meneghini, C. De Santi, I. Abid, M. Buffolo, M. Cioni, R. A. Khadar, L. Nela, N. Zagni, A. Chini, F. Medjdoub, et al. “Gan-based power devices: physics, reliability, and perspectives”. *Journal of Applied Physics* **130**:18 (2021).
- [6] S. Porowski, B. Sadovyi, S. Gierlotka, S. J. Rzoska, I. Grzegory, I. Petrusha, V. Turkevich, and D. Stratiichuk. “The challenge of decomposition and melting of gallium nitride under high pressure and high temperature”. *Journal of Physics and Chemistry of Solids* **85** (2015), pp. 138–143.
- [7] S. Besendörfer, E. Meissner, A. Lesnik, J. Friedrich, A. Dadgar, and T. Erlbacher. “Methodology for the investigation of threading dislocations as a source of vertical leakage in algan/gan-hemt heterostructures for power devices”. *Journal of Applied Physics* **125**:9 (2019).
- [8] T. K. Ng, J. A. Holguin-Lerma, C. H. Kang, I. Ashry, H. Zhang, G. Bucci, and B. S. Ooi. “Group-iii-nitride and halide-perovskite semiconductor gain media for amplified spontaneous emission and lasing applications”. *Journal of Physics D: Applied Physics* **54**:14 (2021), p. 143001.
- [9] R. Delgado Carrascon, S. Richter, M. Nawaz, P. P. Paskov, and V. Darakchieva. “Hot-wall mocvd for high-quality homoepitaxy of gan: understanding nucleation and design of growth strategies”. *Crystal Growth & Design* **22**:12 (2022), pp. 7021–7030.
- [10] K. Grabianska, P. Jaroszynski, A. Sidor, M. Bockowski, and M. Iwinska. “Gan single crystalline substrates by ammonothermal and hve methods for electronic devices”. *Electronics* **9**:9 (2020), p. 1342.

- [11] M. Bockowski, M. Iwinska, M. Amilusik, M. Fijalkowski, B. Lucznik, and T. Sochacki. “Challenges and future perspectives in hve-gan growth on ammonothermal gan seeds”. *Semiconductor Science and Technology* **31**:9 (2016), p. 093002.
- [12] J. Lyons, A. Janotti, and C. Van de Walle. “Effects of carbon on the electrical and optical properties of inn, gan, and aln”. *Physical Review B* **89**:3 (2014), p. 035204.
- [13] D. Koleske, A. Wickenden, R. Henry, and M. Twigg. “Influence of movpe growth conditions on carbon and silicon concentrations in gan”. *Journal of crystal growth* **242**:1-2 (2002), pp. 55–69.
- [14] I. Vurgaftman, J. á. Meyer, and L. R. Ram-Mohan. “Band parameters for iii–v compound semiconductors and their alloys”. *Journal of applied physics* **89**:11 (2001), pp. 5815–5875.
- [15] J. Wu, W. Walukiewicz, W. Shan, K. Yu, J. Ager Iii, S. Li, E. Haller, H. Lu, and W. J. Schaff. “Temperature dependence of the fundamental band gap of inn”. *Journal of Applied Physics* **94**:7 (2003), pp. 4457–4460.
- [16] V. Darakchieva. personal correspondence. 2023.
- [17] H. Selke, V. Kirchner, H. Heinke, S. Einfeldt, P. Ryder, and D. Hommel. “Polytypism in epitaxially grown gallium nitride”. *Journal of crystal growth* **208**:1-4 (2000), pp. 57–64.
- [18] *Wikipedia, howpublished = https://en.wikipedia.org/wiki/gallium_nitride, note = Accessed: 2023-08-08.*
- [19] H. Morkoç. *Handbook of nitride semiconductors and devices, Materials Properties, Physics and Growth*. John Wiley & Sons, 2009.
- [20] J. Wu. “When group-iii nitrides go infrared: new properties and perspectives”. *Journal of applied physics* **106**:1 (2009).
- [21] T. Zimmermann. *Polarisationseffekte in Gruppe-(III)-Nitriden und deren Anwendung in p-Kanal FETs und elektromechanischen Strukturen*. PhD thesis. Universität Ulm, 2008.
- [22] V. Deibuk and A. Voznyi. “Thermodynamic stability and redistribution of charges in ternary algan, ingan, and inaln alloys”. *Semiconductors* **39**:6 (2005), pp. 623–628.
- [23] A. R. Denton and N. W. Ashcroft. “Vegard’s law”. *Physical review A* **43**:6 (1991), p. 3161.
- [24] F. Yun, M. A. Reshchikov, L. He, T. King, H. Morkoç, S. W. Novak, and L. Wei. “Energy band bowing parameter in al x ga 1- x n alloys”. *Journal of applied physics* **92**:8 (2002), pp. 4837–4839.
- [25] O. Katz, B. Meyler, U. Tisch, and J. Salzman. “Determination of band-gap bowing for alxga1–xn alloys”. *physica status solidi (a)* **188**:2 (2001), pp. 789–792.

- [26] A. Reszka, K. P. Korona, S. Tiagulskyi, H. Turski, U. Jahn, S. Kret, R. Bożek, M. Sobanska, Z. R. Zytkeiwicz, and B. J. Kowalski. “Influence of growth polarity switching on the optical and electrical properties of gan/algan nanowire leds”. *Electronics* **10**:1 (2020), p. 45.
- [27] A. Papamichail. *P-type and polarization doping of GaN in hot-wall MOCVD*. PhD thesis. Linköping University Electronic Press, 2022.
- [28] S. M. Sze, Y. Li, and K. K. Ng. *Physics of semiconductor devices*. John wiley & sons, 2021.
- [29] W. Götz, N. Johnson, C. Chen, H. Liu, C. Kuo, and W. Imler. “Activation energies of si donors in gan”. *Applied Physics Letters* **68**:22 (1996), pp. 3144–3146.
- [30] Y. Cao, R. Chu, R. Li, M. Chen, R. Chang, and B. Hughes. “High-voltage vertical gan schottky diode enabled by low-carbon metal-organic chemical vapor deposition growth”. *Applied Physics Letters* **108**:6 (2016).
- [31] C. G. Van de Walle, N. Johnson, and J. Neugebauer. “Hydrogen and acceptor compensation in gan”. In: *Properties, Processing and Applications of Gallium Nitride and Related Semiconductors*. INSPEC, 1999, pp. 317–321.
- [32] J. Tsao, S. Chowdhury, M. Hollis, D. Jena, N. Johnson, K. Jones, R. Kaplar, S. Rajan, C. Van de Walle, E. Bellotti, et al. “Ultrawide-bandgap semiconductors: research opportunities and challenges”. *Advanced Electronic Materials* **4**:1 (2018), p. 1600501.
- [33] T. J. Flack, B. N. Pushpakaran, and S. B. Bayne. “Gan technology for power electronic applications: a review”. *Journal of Electronic Materials* **45** (2016), pp. 2673–2682.
- [34] V. Cimalla, J. Pezoldt, and O. Ambacher. “Group iii nitride and sic based mems and nems: materials properties, technology and applications”. *Journal of Physics D: Applied Physics* **40**:20 (2007), S19.
- [35] A. Barker Jr and M. Ilegems. “Infrared lattice vibrations and free-electron dispersion in gan”. *Physical Review B* **7**:2 (1973), p. 743.
- [36] V. Darakchieva, B. Monemar, and A. Usui. “On the lattice parameters of gan”. *Applied Physics Letters* **91**:3 (2007).
- [37] D. Q. Tran, R. Delgado-Carrascon, J. F. Muth, T. Paskova, M. Nawaz, V. Darakchieva, and P. P. Paskov. “Phonon-boundary scattering and thermal transport in alxgal1-xn: effect of layer thickness”. *Applied Physics Letters* **117**:25 (2020).
- [38] C. J. Richardson and M. L. Lee. “Metamorphic epitaxial materials”. *MRS Bulletin* **41**:3 (2016), pp. 193–198.
- [39] U. W. Pohl. *Epitaxy of semiconductors*. Springer, 2020.
- [40] A. Fischer, H. Kühne, and H. Richter. “New approach in equilibrium theory for strained layer relaxation”. *Physical review letters* **73**:20 (1994), p. 2712.

- [41] Y. C. Liang, G. S. Samudra, and C.-F. Huang. *Power microelectronics: device and process technologies*. World Scientific, 2009.
- [42] E. Miller, E. Yu, P. Waltereit, and J. Speck. “Analysis of reverse-bias leakage current mechanisms in gan grown by molecular-beam epitaxy”. *Applied physics letters* **84**:4 (2004), pp. 535–537.
- [43] S. Ghosh, A. M. Hinz, M. Frentrup, S. Alam, D. J. Wallis, and R. A. Oliver. “Design of step-graded algan buffers for gan-on-si heterostructures grown by movcd”. *Semiconductor Science and Technology* **38**:4 (2023), p. 044001.
- [44] S. Einfeldt, V. Kirchner, H. Heinke, M. Dießelberg, S. Figge, K. Vogeler, and D. Hommel. “Strain relaxation in algan under tensile plane stress”. *Journal of Applied Physics* **88**:12 (2000), pp. 7029–7036.
- [45] J. A. Cuenca, M. D. Smith, D. E. Field, F. C. Massabuau, S. Mandal, J. Pomeroy, D. J. Wallis, R. A. Oliver, I. Thayne, M. Kuball, et al. “Thermal stress modelling of diamond on gan/iii-nitride membranes”. *Carbon* **174** (2021), pp. 647–661.
- [46] T. Kimoto and J. A. Cooper. “Physical properties of silicon carbide” (2014).
- [47] G. Stringfellow. “Thermodynamic aspects of omvpe”. *Journal of Crystal Growth* **70**:1-2 (1984), pp. 133–139.
- [48] P. Gibart. “Metal organic vapour phase epitaxy of gan and lateral overgrowth”. *Reports on Progress in Physics* **67**:5 (2004), p. 667.
- [49] R. Czernecki, K. Moszak, W. Olszewski, E. Grzanka, and M. Leszczynski. “Influence of showerhead–sample distance (gap) in movpe close coupled showerhead reactor on gan growth”. *Materials* **12**:20 (2019), p. 3375.
- [50] S. Irvine and P. Capper. *Metalorganic vapor phase epitaxy (MOVPE): Growth, materials properties, and applications*. John Wiley & Sons, 2019.
- [51] Z. Wang. “On the single-photon-counting (spc) modes of imaging using an xfel source”. *Journal of Instrumentation* **10**:12 (2015), p. C12013.
- [52] J. Als-Nielsen and D. McMorrow. *Elements of modern X-ray physics*. John Wiley & Sons, 2011.
- [53] S. Dolabella, A. Borzi, A. Dommann, and A. Neels. “Lattice strain and defects analysis in nanostructured semiconductor materials and devices by high-resolution x-ray diffraction: theoretical and practical aspects”. *Small Methods* **6**:2 (2022), p. 2100932.
- [54] Q.-J. Xu, B. Liu, S.-Y. Zhang, T. Tao, Z.-L. Xie, X.-Q. Xiu, D.-J. Chen, P. Chen, P. Han, R. Zhang, et al. “Structural characterization of al_{0.55}ga_{0.45}n epitaxial layer determined by high resolution x-ray diffraction and transmission electron microscopy”. *Chinese Physics B* **26**:4 (2017), p. 047801.

- [55] T. Metzger, R. Höpler, E. Born, O. Ambacher, M. Stutzmann, R. Stömmer, M. Schuster, H. Göbel, S. Christiansen, M. Albrecht, et al. “Defect structure of epitaxial gan films determined by transmission electron microscopy and triple-axis x-ray diffractometry”. *Philosophical magazine A* **77**:4 (1998), pp. 1013–1025.
- [56] C. Dunn and E. Kogh. “Comparison of dislocation densities of primary and secondary recrystallization grains of si-fe”. *Acta Metallurgica* **5**:10 (1957), pp. 548–554.
- [57] V. Srikant, J. Speck, and D. Clarke. “Mosaic structure in epitaxial thin films having large lattice mismatch”. *Journal of Applied Physics* **82**:9 (1997), pp. 4286–4295.
- [58] F. J. Giessibl. “Probing the nature of chemical bonds by atomic force microscopy”. *Molecules* **26**:13 (2021), p. 4068.
- [59] N. Jalili and K. Laxminarayana. “A review of atomic force microscopy imaging systems: application to molecular metrology and biological sciences”. *Mechatronics* **14**:8 (2004), pp. 907–945.
- [60] M. H. Korayem, H. J. Sharahi, and A. H. Korayem. “Comparison of frequency response of atomic force microscopy cantilevers under tip-sample interaction in air and liquids”. *Scientia Iranica* **19**:1 (2012), pp. 106–112.
- [61] J. Canet-Ferrer, E. Coronado, A. Forment-Aliaga, and E. Pinilla-Cienfuegos. “Correction of the tip convolution effects in the imaging of nanostructures studied through scanning force microscopy”. *Nanotechnology* **25**:39 (2014), p. 395703.
- [62] P. Van der Heide. *Secondary ion mass spectrometry: an introduction to principles and practices*. John Wiley & Sons, 2014.
- [63] D. B. Williams, C. B. Carter, D. B. Williams, and C. B. Carter. *The transmission electron microscope*. Springer, 1996.
- [64] Wikipedia, howpublished = https://en.wikipedia.org/wiki/atomic_force_microscopy, note = Accessed: 2023-08-08.
- [65] Wikipedia, howpublished = <https://www.gems-inclusions.com/inclusions-studies/analytical-methods/sem-eds-wds-analysis/>, note = Accessed: 2023-08-08.
- [66] M. Scimeca, S. Bischetti, H. K. Lamsira, R. Bonfiglio, and E. Bonanno. “Energy dispersive x-ray (edx) microanalysis: a powerful tool in biomedical research and diagnosis”. *European journal of histochemistry: EJH* **62**:1 (2018).
- [67] D. Koleske, R. M. Biefeld, and J. G. Cederberg. *The Science and Practice of Metal-Organic Vapor Phase Epitaxy (MOVPE)*. Tech. rep. Sandia National Lab.(SNL-NM), Albuquerque, NM (United States), 2014.

- [68] M. Bakhtiary-Noodeh, T. Detchprohm, and R. D. Dupuis. “Carbon and silicon background impurity control in undoped gan layers grown with trimethylgallium and triethylgallium via metalorganic chemical vapor deposition”. *Journal of Crystal Growth* **602** (2023), p. 126982.
- [69] Y. Inatomi, Y. Kangawa, A. Pimpinelli, and T. Einstein. “Kinetic-thermodynamic model for carbon incorporation during step-flow growth of gan by metalorganic vapor phase epitaxy”. *Physical Review Materials* **3**:1 (2019), p. 013401.
- [70] D. Koleske, A. Wickenden, R. Henry, J. Culbertson, and M. Twigg. “Gan decomposition in h₂ and n₂ at mophe temperatures and pressures”. *Journal of crystal growth* **223**:4 (2001), pp. 466–483.
- [71] A. Ariff, M. Ahmad, Z. Hassan, and N. Zainal. “Influence of ammonia flow rate for improving properties of polycrystalline gan”. *Superlattices and Microstructures* **118** (2018), pp. 130–136.
- [72] S. Fritze, A. Dadgar, H. Witte, M. Bügler, A. Rohrbeck, J. Bläsing, A. Hoffmann, and A. Krost. “High si and ge n-type doping of gan doping-limits and impact on stress”. *Applied Physics Letters* **100**:12 (2012).
- [73] Z. Ye, S. Nitta, K. Nagamatsu, N. Fujimoto, M. Kushimoto, M. Deki, A. Tanaka, Y. Honda, M. Pristovsek, and H. Amano. “Ammonia decomposition and reaction by high-resolution mass spectrometry for group iii–nitride epitaxial growth”. *Journal of Crystal Growth* **516** (2019), pp. 63–66.
- [74] M. Liang, G. Wang, H. Li, Z. Li, R. Yao, B. Wang, P. Li, J. Li, X. Yi, J. Wang, et al. “Low threading dislocation density in gan films grown on patterned sapphire substrates”. *Journal of Semiconductors* **33**:11 (2012), p. 113002.
- [75] A. Khan, K. Balakrishnan, and T. Katona. “Ultraviolet light-emitting diodes based on group three nitrides”. *Nature photonics* **2**:2 (2008), pp. 77–84.
- [76] V. Stanishev, N. Armakavicius, D. Gogova, M. Nawaz, N. Rorsman, P. P. Paskov, and V. Darakchieva. “Low al-content n-type alxga1-xn layers with a high-electron-mobility grown by hot-wall metalorganic chemical vapor deposition”. *Vacuum* (2023), p. 112481.
- [77] L. Romano, C. Van de Walle, J. Ager III, W. Götz, and R. Kern. “Effect of si doping on strain, cracking, and microstructure in gan thin films grown by metalorganic chemical vapor deposition”. *Journal of Applied Physics* **87**:11 (2000), pp. 7745–7752.
- [78] A. Kondratyev, R. Talalaev, W. Lundin, A. Sakharov, A. Tsatsul’nikov, E. Zavarin, A. Fomin, and D. Sizov. “Aluminum incorporation control in algan mophe: experimental and modeling study”. *Journal of crystal growth* **272**:1-4 (2004), pp. 420–425.

Bibliography

- [79] Y. Feng, V. Saravade, T.-F. Chung, Y. Dong, H. Zhou, B. Kucukgok, I. T. Ferguson, and N. Lu. “Strain-stress study of $\text{Al}_x\text{Ga}_{1-x}\text{N}/\text{AlN}$ heterostructures on c-plane sapphire and related optical properties”. *Scientific reports* **9**:1 (2019), p. 10172.
- [80] Y. Zhang, Z. Chen, W. Li, A. R. Arehart, S. A. Ringel, and H. Zhao. “Metalorganic chemical vapor deposition gallium nitride with fast growth rate for vertical power device applications”. *physica status solidi (a)* **218**:6 (2021), p. 2000469.